Remote Sensing of Environment 331 (2025) 115006

Contents lists available at ScienceDirect

Remote Sensing of Environment

journal homepage: www.elsevier.com/locate/rse

The NASA VIIRS burned area product, global validation, and intercomparison with the NASA MODIS burned area product

Louis Giglio [a,*], Luigi Boschetti [b], David P. Roy [c], Joanne V. Hall [a], Maria Zubkova [a], Michael Humber [a], Haiyan Huang [c], Vladyslav Oles [b]

[a] Department of Geographical Sciences, University of Maryland, College Park, MD 20740, USA
[b] Department of Forest, Rangeland and Fire Sciences, University of Idaho, Moscow, ID 83843, USA
[c] Center for Global Change and Earth Observations, and Department of Geography, Environment, & Spatial Sciences, Michigan State University, East Lansing, MI 48824, USA

ARTICLE INFO

Edited by Zhe Zhu

Keywords:
Fire
Biomass burning
Burned area
VIIRS
VNP64A1

ABSTRACT

The VIIRS was designed in recognition of the need for long-term observations in support of global-change science and to provide MODIS observation continuity. The NASA MODIS burned area (BA) product (MCD64A1) has been generated systematically for nearly 25 years and maps globally the approximate day of burning at 500-m resolution. We describe the follow-on NASA Collection 2 VIIRS BA product (VNP64A1) that became available in October 2024 and provides global BA mapping from 2012 into the next decade. The product is derived using an adaptation of the Collection 6.1 MCD64A1 BA mapping algorithm and using the same sinusoidal grid and 500-m reporting resolution. Annual and monthly intercomparisons of the VPN64A1 and MCD64A1 products at global and continental/regional scales indicate high product BA reporting consistency. Approximately 2.6 % of the land surface was mapped as burned annually; VNP64A1 mapped slightly more than MCD64A1 but with 0-day median burn-date reporting differences. A global (Stage-3) product validation, using 561 interpreted Landsat image pairs, was undertaken and the VNP64A1 product had estimated 36.7 % commission and 72.4 % omission errors, compared to MCD64A1 34.2 % commission and 71.5 % omission errors. Product accuracies were also characterized using metrics derived from the weighted regression (to incorporate sample inclusion probabilities) between 5-km BA proportions in the products and the Landsat data. The omission and commission errors observed at 30-m were largely compensated at 5-km, with coefficient of determination (0.70), slope (0.83), and intercept (−0.0006) terms for the VNP64A1 product nearly identical to those of MCD64A1. With respect to global temporal reporting accuracy, 38 % of VNP64A1 burned grid cells had burn dates that matched the date of a MODIS active fire, versus 46 % for MCD64A1, and 71 % of VNP64A1 burned grid cells had burn dates within two days (72 % for MCD64A1). The research presented in this paper indicates that the VNP64A1 product is suitable for providing continuity of the MODIS BA record.

1. Introduction

In the last several decades, regions worldwide are being subject to increasingly severe wildfires with longer fire seasons associated with climate and land use change (Keeley and Syphard, 2021; Collins et al., 2022; Ellis et al., 2022; Jones et al., 2022). Fire is an important ecological process and plays a major role in the terrestrial carbon cycle, contributing significantly to carbon emissions (van der Werf et al., 2017) and influencing atmospheric chemistry and dynamics. Global coverage and temporally resolved satellite observations are needed for wildfire monitoring due to the unpredictable nature of fire location and timing, as well as the rapid changes in fire behavior that can occur once a fire ignites (Roy et al., 2024). Satellite burned area (BA) products map the spatial extent of the fire-affected area, and the approximate date of burning, typically by examination of changes in time-resolved surface reflectance and/or derived spectral indices (Roy et al., 2005; Giglio et al., 2018; Lizundia-Loiola et al., 2020). BA is recognized as a Global Climate Observing System (GCOS) Essential Climate Variable (ECV) (Bojinski et al., 2014), and a consistent multi-decadal global BA record is needed to identify trends and disentangle the impact of human activity

* Corresponding author.
E-mail address: lgiglio@umd.edu (L. Giglio).

https://doi.org/10.1016/j.rse.2025.115006
Received 22 July 2025; Received in revised form 29 August 2025; Accepted 2 September 2025
Available online 10 September 2025

and climate change on fire occurrence and behavior (Giglio and Roy, 2020).

The Moderate Resolution Imaging Spectroradiometer (MODIS) was deployed in 1999 and 2002 on the Terra and Aqua polar orbiting satellites and was the first global-coverage sensor to include capabilities designed specifically for fire monitoring (Justice et al., 2002). However, the two MODIS sensors are past their mission design lives and are currently scheduled to be decommissioned in 2026. The Visible Infrared Imaging Radiometer Suite (VIIRS) onboard the polar orbiting S-NPP, NOAA-20, and NOAA-21 satellites, launched in 2012, 2017, and 2022 respectively, was designed to provide long-term observations in support of global-change science and MODIS observation continuity (Justice et al., 2013). In preparation for the decommissioning of the Terra and Aqua satellites, NASA initiated an effort to develop a suite of S-NPP VIIRS Land products to be consistent with and potentially superior to the established base of NASA MODIS Land products (Román et al., 2024). Included in this suite is a NASA VIIRS BA product (VNP64A1) that aims to continue the long-term NASA MODIS BA product (MCD64A1) product that has been generated systematically for nearly 25 years and maps the approximate day of burning at 500-m resolution (Giglio et al., 2018).

The VNP64A1 product began production in 2019 as part of the Collection 1 (C1) VIIRS standard product suite. The product was not released, however, because of a preponderance of BA commission errors found by systematic product quality assessment. The commission errors were traced to ~5-km blocky artifacts in the upstream C1 VIIRS cloud mask that were in turn caused by a 0.05° gridded ancillary climatological input data set. These issues were rectified and the VIIRS standard product suite was reprocessed in late 2023 as Collection 2 (C2). The C2 VNP64A1 product became available publicly in October 2024 and maps the approximate day of burning at 500-m resolution globally.

In this paper we describe the VNP64A1 product and the results of a comprehensive accuracy assessment, beginning with a description of the product in Section 2. Section 3 discusses VIIRS-MODIS differences and summarizes the changes that were necessary to adapt the most recent Collection 6.1 (C6.1) MODIS MCD64A1 algorithm to the VIIRS sensor data stream. Section 4 provides a multi-temporal assessment of VNP64A1/MCD64A1 product consistency, and Section 5 presents the global validation results for both products using independent reference BA data. The paper concludes with discussion and considerations on the likely need for regional-scale statistical calibration of the VNP64A1 and MCD64A1 BA products to provide a single long-term, consistent fire record.

2. VIIRS burned area product description

2.1. VNP64A1 product characteristics and overview

The NASA VIIRS BA product (VNP64A1), like the MODIS MCD64A1 predecessor (Giglio et al., 2018), identifies the approximate day of burning at 500-m resolution and is defined in fixed approximately 1100 km × 1100 km (10° × 10° at the equator) non-overlapping geolocated tiles in the sinusoidal equal-area projection (Wolfe et al., 1998). While the native spatial resolution of the VIIRS bands used to generate the VNP64A1 product is coarser than the 500-m MODIS bands used to generate the legacy MCD64A1 product, for compatibility the VNP64A1 product is generated on the same 500-m sinusoidal grid in the same HDF4 file format used for all standard MODIS products. The product is generated globally, excluding Antarctica, over emersed lands from 80°N to 60°S. The VNP64A1-detected burn date is encoded for each gridded 500-m tile cell as the ordinal day of the calendar year (range 1–366), with a value of 0 if no burning was detected, and values of −1 and − 2 to denote missing data (unknown burn status) and water presence, respectively. Additional data layers are described in detail in the VNP64A1 product User Guide (Giglio et al., 2024) and are included for technical product use, to facilitate uncertainty propagation into downstream products that use VNP64A1, and for quality assessment purposes.

Fig. 1 shows the VNP64A1 product for a global 12-month period. A May 2023 through April 2024 period is illustrated to capture the peak burning seasons around the world and to avoid reporting artifacts found when showing a global calendar year period. For example, Northern Africa and Northern South America have peak burning seasons around December through January, so a calendar year definition may be inappropriate as the fire season is split between calendar years (Boschetti and Roy, 2008). The global extent of burning is evident, particularly in savanna systems in Southern America, Africa, and Australia, where an annual rainy season and a long dry season produce ideal fire conditions, and across North America and Eurasia, where boreal forest fires are often extensive due to dry and high fuel loads.

Fig. 2 shows two example VNP64A1 tiles mapped for August 2023 over Southern Africa (left) and for October 2023 over Northern Australia (right). These regions have frequent and extensive burning but different characteristic BA spatial arrangements due to differences in the biophysical and anthropogenic factors that drive and constrain fire (Archibald et al., 2009; Edwards et al., 2015).

2.2. VNP64 product availability and access

The C2 VNP64A1 product is generated on a dedicated high-performance computing infrastructure, at NASA's Goddard Space Flight Center, on the same NASA Land Science Investigator-led Processing System (SIPS) used to generate the MODIS Land products (Masuoka et al., 2011; Román et al., 2024). The product generation is undertaken on a systematic basis and is supported with routine product quality assessment.

The C2 VNP64A1 product is publicly available, with global coverage from March 2012 to present day, and will be produced systematically over the life of the overarching multi-satellite NOAA/NASA Joint Polar Satellite System (JPSS) mission into the 2030s. Specifically, the product is available from NASA's Land Processes Distributed Active Archive Center (DAAC) (https://lpdaac.usgs.gov/products/vnp64a1v002/) and NASA's Level-1 and Atmosphere Archive & Distribution System (LAADS) DAAC (https://ladsweb.modaps.eosdis.nasa.gov/).

3. VIIRS burned area mapping algorithm

The VIIRS mapping approach is a straightforward adaptation of the existing MODIS MCD64A1 BA mapping algorithm. The VIIRS input data streams are described in Section 3.1, and the mapping approach is briefly summarized for completeness in Section 3.2. Section 3.3 provides more detail about VIIRS and MODIS differences in the context of the MCD64A1 algorithm. Unless explicitly noted in Section 3.4, which presents a detailed discussion of the VIIRS algorithm adjustments, all algorithm implementation details (e.g., processing steps, formulae, numerical thresholds) are as in Giglio et al. (2009, 2018), where the

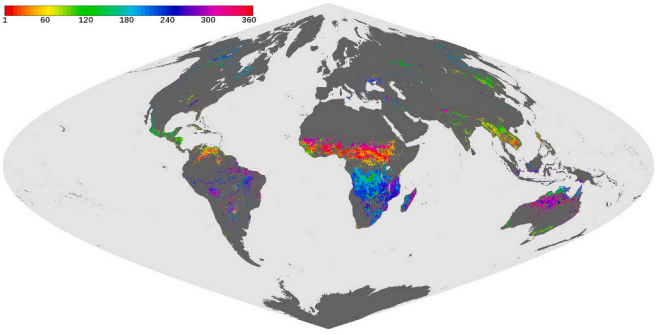

Fig. 1. Annual VIIRS burned area map for the 12-month period from May 2023 through April 2024, showing the mapped day of burning colored with a chronological rainbow color scale, unburned land in dark grey, and water in light grey.

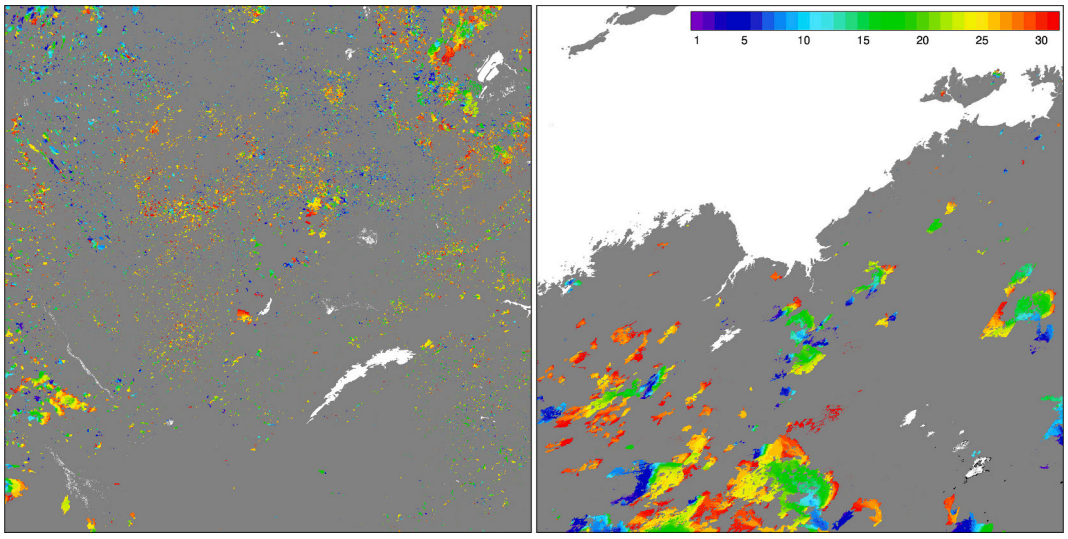

Fig. 2. Monthly VIIRS burned area maps for 1100 km × 1100 km tiles located in Southern Africa (tile h20v10, left panel) and northern Australia (tile h30v10, right panel) for August 2023 and October 2023, respectively. The day of burn during each month (range 1–31) is depicted using a rainbow color scale (inset). Unburned land areas are shown in dark grey, water is shown in white, and cells that were unmapped (due to a lack of valid surface reflectance observations) are shown in black.

algorithm is described in detail.

3.1. VIIRS overview and input data

The VNP64A1 product is derived from the S-NPP VIIRS data stream and using the C6.1 MODIS MCD64A1 algorithm (Giglio et al., 2018) with adjustments to accommodate the different VIIRS and MODIS satellite orbits and sensor characteristics. The S-NPP satellite is in a sun-synchronous polar circular 830-km orbit with a 13:30 local equator daytime crossing time (Justice et al., 2013). The Terra and Aqua satellites are in sun-synchronous polar circular 705-km orbits with local equator daytime crossing times of 10:30 and 13:30, respectively (Justice et al., 1998). The MODIS MCD64A1 product is derived from the Terra and Aqua MODIS data streams which together acquire more daytime observations than the S-NPP VIIRS, since the Terra MODIS acquires morning observations that are not provided by VIIRS. However, the higher VIIRS orbit and 113° field of view provides a 3060-km swath allowing the entire Earth's surface to be sensed by VIIRS daily (Justice et al., 2013), whereas the lower Terra and Aqua orbits and MODIS 110° field of view provide a 2330-km swath that senses the Earth daily only at latitudes >30°, making it necessary to combine Terra and Aqua observations to achieve full daily global coverage (Wolfe et al., 1998). MODIS uses an older whiskbroom scanner architecture, and the ground area sensed by each MODIS detector increases rapidly further from nadir at greater view zenith angles (Wolfe et al., 1998); VIIRS uses a more sophisticated version of the MODIS architecture with an across-track sawtooth detector aggregation scheme to limit this increase (Wolfe et al., 2013). Thus, at the MODIS swath-edge a detector senses a ground area about 9.7 times greater than at nadir (Wolfe et al., 1998), whereas at the VIIRS swath-edge a detector senses a ground area only about 3.3 times greater than at nadir (Schroeder et al., 2014). These and other differences have implications for VIIRS BA mapping (Section 3.3) and the consistency of the MODIS and VIIRS BA products (Section 4).

As with the MODIS MCD64A1 BA product, three months of daily S-NPP VIIRS observations are used to map the central month. The processing is undertaken independently for each 1100 km × 1100 km tile. Fig. 3 summarizes the main steps of the BA mapping algorithm and the three required input data streams (shown in light grey). The C2 S-NPP VIIRS 500-m atmospherically corrected Level-2G daily surface reflectance product (VNP09GHKM) is the main algorithm input. The surface reflectance data are derived using the same 6SV radiative transfer approach used for MODIS and are resampled from the VIIRS native 750-m resolution onto the standard 500-m MODIS sinusoidal grid (Roger et al., 2023). To match the MODIS MCD64A1 algorithm as closely as possible, only the 0.67 μm (red), 1.24 μm (near-infrared), and 2.25 μm (shortwave infrared) surface reflectance bands are used (VIIRS bands M5, M8, and M11, respectively). The 0.67 μm channel is used only in rare cases to override the VNP09 per-pixel cloud mask associated with cloud commission errors related to wet soils that can confuse the burned area mapping. Specifically, bit patterns of 11 (confident cloudy) and 10 (probably cloudy) in the VNP09 "cloud detection and confidence" field (bits 2–3) are replaced with bit pattern 00 (confident clear) when the 0.67 μm reflectance is <0.02. The 1-km C2 S-NPP VIIRS Level-3 daily gridded active fire product (VNP14A1) that resamples the 750-m product pixels onto the standard 1-km MODIS sinusoidal grid (Giglio, 2023) is also used as an input to the VIIRS-adapted BA algorithm. In addition, the annual Collection-5.1 500-m Level 3 MODIS global land cover product (MCD12Q1; Friedl et al., 2010) is used (13-class University of Maryland classification scheme) since NASA does not currently produce an equivalent VIIRS land cover product.

3.2. Burned area mapping algorithm

The algorithm proceeds through a sequence of stages as broadly depicted in Fig. 3. The general approach is to generate three-month temporal composites that capture persistent changes in a time series of a burn-sensitive normalized vegetation index. Spatial and temporal active-fire detection information is subsequently used to inform the statistical characterization of burn-related and non-burn-related changes by estimating probabilistic thresholds to label individual 500-m grid cells as *burned*, *unburned*, or in comparatively rare instances (e.g., during very long periods of persistent cloud cover) as *unclassified*.

The algorithm begins by extracting valid (cloud-free, fire-free, acquired over land) daily 0.67 μm, 1.24 μm, and 2.25 μm surface reflectance values for the three-month period encompassing the central calendar month being mapped. To minimize bi-directional reflectance effects, if multiple valid observations are available at a given 500-m location on a given day, then the one sensed with the smallest view zenith angle is selected. A daily burn-sensitive spectral index (henceforth, VI), defined as the normalized ratio of the 1.24 μm and 2.25 μm bands, is then computed.

Next, change- and fire-related summary image composites are generated for subsequent classification. During this phase, the daily VI series at each tile grid cell location (x,y) is examined by considering

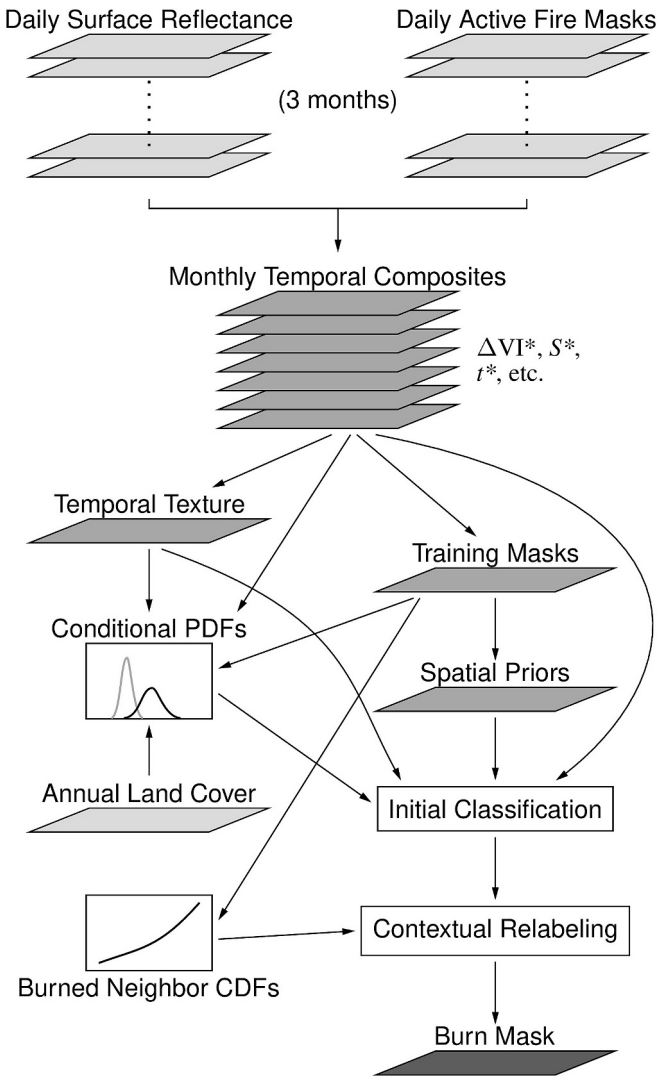

Fig. 3. Flow chart of the VIIRS burned area mapping algorithm as applied to individual 1100 km × 1100 km tiles defined in the sinusoidal projection. Input data layers are shown in light grey, intermediate data layers computed internally are shown in medium grey, and the final output map is shown in dark grey.

observations within two non-overlapping, adjacent sliding temporal windows, referred to as the *candidate pre-burn* and *candidate post-burn* windows, each containing 8 consecutive daily observations. Robust descriptive statistics (the 10 % trimmed mean and trimmed standard deviation, which exclude the smallest and largest tenth of observations) are computed at each temporal position k both for the candidate pre-burn and candidate post-burn windows, and are then used to compute a daily measure of pre- and post-burn VI separability, $S(x,y,k)$, defined as:

$$S(x,y,k) = \frac{\Delta \mathrm{VI}(x,y,k)}{\left[\sigma_{\mathrm{pre}}(x,y,k) + \sigma_{\mathrm{post}}(x,y,k)\right]/2} \quad (1)$$

where $\Delta \mathrm{VI}(x,y,k)$ is the difference between the trimmed mean of the candidate pre-burn and post-burn windows, and $\sigma_{\mathrm{pre}}(x,y,k)$ and $\sigma_{\mathrm{post}}(x,y,k)$ are the trimmed standard deviations of the pre-burn and post-burn windows, respectively.

From this derived time series S, the date of maximum VI separability $t^*(x,y)$ is determined and used to generate image composites composed of nine metrics (cf. Giglio et al., 2018, Table 1) summarizing for each grid cell (x,y): (*i*) the maximum separability $S^*(x,y,t^*)$, (*ii*) the maximum VI change $\Delta \mathrm{VI}^*(x,y,t^*)$, (*iii*) the post maximum-separability mean VI, (*iv*) the date of maximum separability, (*v*) its uncertainty, (*vi*, *vii*) the interquartile range of observation dates in the candidate pre-burn and post-burn windows associated with the maximum separability, (*viii*) a measure of *temporal texture* $\sigma_t^*(x,y)$ defined as the rank-filtered local standard deviation of t^* within a small kernel centered on the grid cell, and (*ix*) the cumulative active fire mask that reports for each grid cell the date on which an active fire was detected (if any).

Table 1
Annual total global burned area reported by the VNP64A1 and MCD64A1 BA products for 2012–2023, VNP64A1-MCD64A1 BA annual difference relative to MCD64A1 (Δ), and 0.25° regression slope and Pearson correlation coefficient (r). Entries for 2012 are for the 10-month period from March through December.

	Burned Area (Mha)				
Year	VNP64A1	MCD64A1	Δ	slope	r
2012	399.7	390.1	2.5 %	1.02	0.982
2013	378.5	356.1	6.3 %	1.04	0.980
2014	392.7	381.6	2.9 %	1.01	0.973
2015	403.7	384.9	4.9 %	1.02	0.979
2016	382.8	365.7	4.7 %	1.02	0.983
2017	395.8	387.5	2.1 %	1.01	0.977
2018	370.9	354.2	4.7 %	1.03	0.981
2019	358.3	345.7	3.6 %	1.02	0.979
2020	359.4	351.1	2.4 %	1.01	0.978
2021	364.6	353.6	3.1 %	1.01	0.983
2022	351.9	331.3	6.2 %	1.04	0.973
2023	407.5	384.1	6.1 %	1.03	0.977

Next, selected grid cells are labeled a priori as *unburned* if their maximum pre- and post-burn VI separability is too low ($S^*(x,y,t^*) < 2$) or their temporal texture is too high ($\sigma_t^*(x,y) > 7.5$ days; note that high σ_t^* implies low temporal coherence) to be compatible with the behavior of a burned patch. The cumulative active fire mask, after undergoing a process of cleaning and region growing, is then used to generate a burned training mask that identifies representative burned training cells for the tile during the three-month period. A complementary unburned training mask is composed of cells that were labeled a priori as *unburned* or are sufficiently distant (> ~9 km) from the nearest grid cell within the burned training mask. All grid cells within the respective training masks are subsequently used to derive conditional burned (B) and unburned (U) VI probability density functions (PDFs) for each land cover type (l) present in the tile.

In preparation for the application of a Bayesian classification rule, prior spatial burned probabilities $P_{\mathrm{B}}(x,y)$ are established as an exponentially decreasing function (Giglio et al., 2009, 2018) of the distance between each grid cell's location and the nearest burned training cell, where $P_{\min} \le P_{\mathrm{B}}(x,y) \le P_{\max} = 0.5$, with $P_{\min}$ to be specified in Section 3.4. With this prior and the conditional PDFs obtained earlier, the posterior probability $P_l(\mathrm{B}|\Delta \mathrm{VI}^*(x,y))$ of the grid cell having burned during the compositing period, given the observed change in the VI, is then calculated.

In conjunction with additional tests, each grid cell is tentatively classified as *burned* if $P_l(\mathrm{B}|\Delta \mathrm{VI}^*(x,y)) \ge P_{\mathrm{M}}$, where P_{M} is a minimum threshold (see Section 3.4 for the VIIRS-specific threshold implementation), otherwise it is tentatively classified as *unburned*.

In a final contextual step, all classified grid cells are re-examined for potential relabeling (from *burned* to *unburned*, or vice versa) based on the local cumulative conditional probability that a burned grid cell has n_{B} or fewer burned neighboring grid cells, $F(n_{\mathrm{B}}|\mathrm{B})$. This cumulative probability is estimated independently for each tile grid cell that was tentatively classified as either *burned* or *unburned,* based on examining the surrounding neighborhood grid cells and using the burned training mask as a proxy burned area map. This relabeling scheme is equivalent to a majority filter with constraints to avoid removing isolated burned pixels indiscriminately.

3.3. VIIRS-MODIS differences

As noted in Section 3.1, the VIIRS and MODIS BA products use different sensor data that complicate the production of a VIIRS-based product that is consistent with its MODIS precursor. First, the spectral placement of two of the three bands used by the algorithm differs between the sensors. The VIIRS and MODIS have the same 1.230–1.250 μm short-wave infrared (SWIR) band. However, the other SWIR band used by the algorithm is situated at a longer wavelength for VIIRS (2.225–2.275 μm) compared to MODIS (2.105–2.155 μm) (Justice et al., 2010) and consequently alters the VI time series that is derived and processed by the mapping algorithm. The VIIRS red band (0.662–0.682 μm) also differs from the MODIS red band (0.620–0.670 μm) (Román et al., 2024), although as noted above this band is only used in rare instances. Second, native 750-m VIIRS swath pixels are coarser than 500-m MODIS swath pixels, although this disparity is partially offset by the constrained along-scan VIIRS pixel growth. Third, the 3060-km VIIRS swath provides greater spatial coverage than the 2330-km MODIS swath but acquires observations over a greater range of view zenith angles due to Earth curvature and the wider VIIRS field of view (e.g., Fig. 4 solid lines). Bidirectional reflectance effects typically increase over both burned and unburned surfaces at higher view zenith angles (Roy et al., 2002) and can be characterized with a bidirectional reflectance distribution function (BRDF). The moving-average temporal windows used in the mapping algorithm and the daily gridded surface reflectance compositing help to reduce the VIIRS view zenith angle range (Fig. 4, dashed lines). However, VIIRS has a longer orbital repeat cycle than the effective repeat cycle of MODIS on Terra and Aqua combined (i.e., Fig. 4 top and center dashed-line oscillations), which varies latitudinally, and so the 8-day temporal windows retained from the original MODIS algorithm do not fully suppress the VIIRS BRDF effects. Lengthening this temporal window for VIIRS only would have the unwanted effect of aggravating temporal and potentially spatial discrepancies between the final products through, for example, larger errors in the reported burn date, or by decreasing the maximum VI separability S^* (Section 3.2) as the variability within the window becomes increasingly dominated by gradual (e.g., seasonal) changes in the daily VI time series. The reduced separability would ultimately produce more omission errors and fewer commission errors in the BA product. A vastly better alternative to window adjustment is to use S-NPP and NOAA-20 VIIRS observations in combination (Fig. 4, bottom dashed-line), exploiting the deliberate orbital phasing of the two satellites.

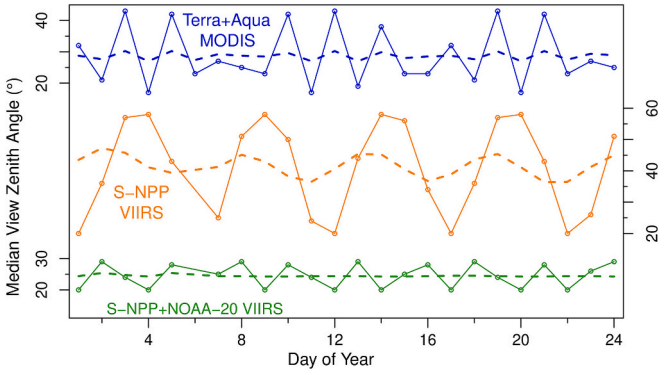

Fig. 4. Median view zenith angle of the daily surface reflectance selected by the compositing algorithm for the first 24 days of 2020 in tile h20v10 (southern Africa; see Fig. 2 left panel) for Terra + Aqua MODIS in combination (blue line), S-NPP VIIRS alone (orange line), and S-NPP + NOAA-20 VIIRS in combination (green line). The dashed lines replicate the effect of the trimmed moving average used to construct the candidate pre- and post-burn temporal windows used by the burned area mapping algorithm (Section 3.2). (For interpretation of the references to color in this figure legend, the reader is referred to the web version of this article.)

This two-sensor configuration, which we revisit in Section 6, was unfortunately not an option for the C2 VNP64A1 product due to the heavy processing burden currently placed on NASA's VIIRS land processing system.

A fourth difference that complicates production of a consistent VIIRS-based successor BA product occurs as a consequence of the sensor pixel size and view zenith-angle sampling differences. These issues together cause sub-pixel spatial resampling errors when the native swath surface reflectance observations are resampled into the sinusoidal grid and then composited (Roy, 2000; Tan et al., 2006). Fifth, the S-NPP satellite crosses the equator at 1:30/13:30, like Aqua, whereas the Terra satellite crosses the equator three hours earlier at 10:30/22:30. This is primarily an issue because fires can occur throughout the day and night (Giglio, 2007), and so VIIRS may undersample the diurnal variation in fire activity compared to MODIS on Terra and Aqua (Román et al., 2024; Roy et al., 2024).

3.4. VIIRS algorithm adjustments

In formulating specific algorithm adjustments for the VIIRS sensor, sensitivity analyses (not shown) were undertaken to help ascertain the degree to which selected algorithm parameters influenced the agreement between the VIIRS and MODIS mapped BA results. Based in part upon these analyses and exploratory adjustments coupled with close inspection of intermediate algorithm outputs, the following minor changes were made to the MCD64A1 mapping algorithm to adapt it for VIIRS implementation:

1. The threshold applied to the temporal texture during the selection of unburned training samples was reduced from 8 days (cf. Giglio et al., 2018, Section 3.4.1) to 7.5 days. This adjustment reflects the slight differences in spatial consistency of S-NPP VIIRS observations compared to Terra + Aqua MODIS, due to the residual BRDF effects discussed above (Fig. 4).
2. The morphological erosion used in isolating a clean subset of active-fire cells was slightly relaxed to eliminate fewer candidates. Specifically, whereas the original MODIS algorithm requires all N fire-mask neighbors to be set for a candidate burned training cell to avoid rejection (cf. Giglio et al., 2018, Section 3.4.2), for VIIRS this criterion was reduced to N-1. This adjustment accommodates the sparser blanketing of larger burned patches by 750-m VIIRS fire pixels that results from the sensor's constrained pixel growth in combination with the subsequent resampling to the fixed 1-km MODIS sinusoidal grid.
3. The minimum prior burned probability P_{min} assigned to grid cells that are far from the proximity of burned training cells was decreased from 0.01 (cf. Giglio et al., 2018, Section 3.7) to 0.005. This adjustment was originally made to reduce the impact of artifacts in the C1 VIIRS cloud-mask (Section 1) but was conservatively retained for C2.

4. VNP64A1/MCD64A1 product consistency

To broadly assess product consistency, the C2 VNP64A1 and C6.1 MCD64A1 BA products were compared after aggregating the products spatially at the 0.25° resolution of the MODIS Climate Modeling Grid (Giglio et al., 2022) and aggregating temporally by calendar month. In addition, the reported day of burning for both products was compared at the native product resolutions.

4.1. Global consistency

4.1.1. Global spatial consistency

Fig. 5 shows the 11-year (2013−2023) mean annual VNP64A1 and MCD64A1 BA, aggregated at 0.25° grid cell resolution. The spatial agreement between the products at this scale is high, reflected by a

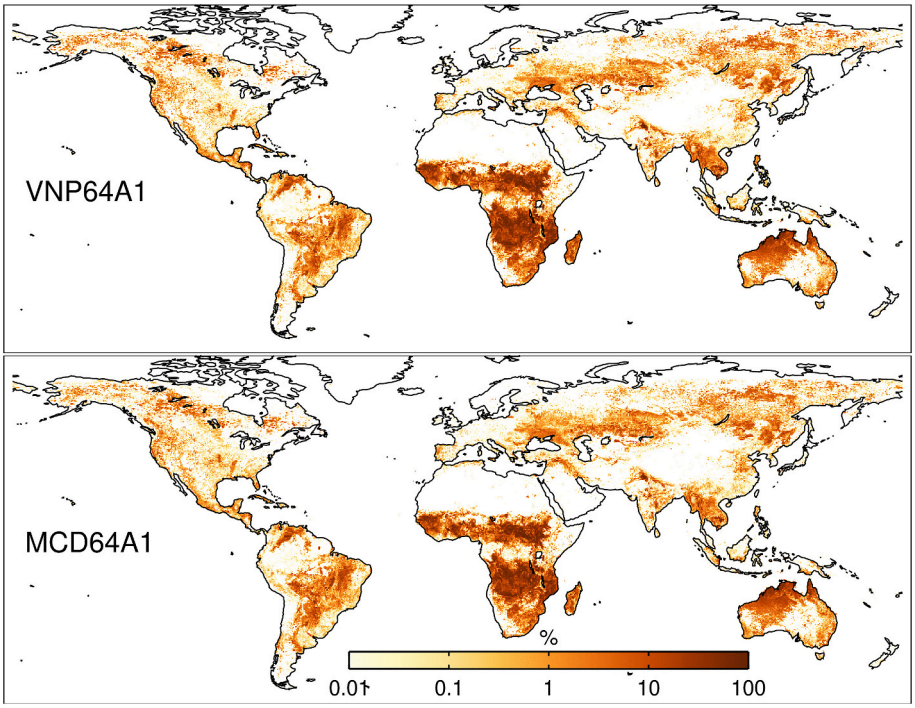

Fig. 5. Gridded mean annual VNP64A1 (top panel) and MCD64A1 (bottom panel) burned area for years 2013–2023, inclusive, depicted as the fraction of each 0.25° grid cell that burned each year.

Pearson correlation coefficient of $r = 0.991$. However, caution should be used when interpreting this high correlation, as burned area omission and commission errors may compensate each other with progressively coarser grid cells (Boschetti et al., 2019), and high product agreement evaluated at coarse grid resolution might be observed even in cases where the two products map burns at different locations within the grid cell (Roy et al., 2019).

Table 1 summarizes the total annual BA mapped globally by VNP64A1 and MCD64A1 from 2012 to 2023. The mean annual BA over this period is 386.0 Mha and 370.9 Mha for VNP64A1 and MCD64A1, respectively, and corresponds to approximately 2.6 % of the land surface. Annually, the VNP64A1 product consistently mapped more global BA than MCD64A1, by a low of 2.1 % in 2017 to a high of 6.3 % in 2013.

Fig. 6 shows the annual spatial consistency of VNP64A1 versus MCD64A1 BA at 0.25° grid-cell resolution visually and in terms of the Pearson coefficient of correlation and the slope of the orthogonal least-squares linear regression (Glaister, 2001), which allows error in both the VNP64A1 and MCD64A1 BA estimates. Both regression parameters are included in Table 1 (y-intercepts were permitted in the linear model but were effectively zero for all years and hence are not shown). The spatial coherence of the annual BA mapped by the two products was high, with a correlation coefficient varying from 0.973 (2014 and 2022) to 0.983 (2016 and 2021). The orthogonal least-squares linear regression slope was slightly above unity for all years, ranging from 1.01 to 1.04, consistent with the tendency of VNP64A1 to overestimate BA relative to MCD64A1. The unusual patch of errant cells in 2014 (Fig. 6, top right panel) that hug the horizontal axis reflect an anomalous month of MCD64A1 commission errors in southeast Russia and will be discussed in Section 4.2.2.

4.1.2. Global temporal consistency

The products were globally consistent at the monthly temporal scale from March 2012 through December 2023 (Fig. 7). Over the 142 months, the global monthly BA totals had a Pearson correlation coefficient of 0.989. The mean absolute monthly VNP64A1 - MCD64A1 BA difference was 1.27 Mha, and the mean monthly relative difference ([VNP64A1 - MCD64A1]/MCD64A1) was 5.3 %. The two largest absolute discrepancies between the BA time series that occur in August 2020 (8.28-Mha difference) and August 2022 (8.31-Mha difference) coincide with two periods of extended 15-day Aqua MODIS and 16-day S-NPP VIIRS sensor outages in August 2020 and July–August 2022, respectively.

Fig. 8 shows the Pearson correlation between the VNP64A1/MCD64A1 monthly BA time series within each 0.25° grid cell for the period from March 2012 through December 2023. The agreement between the time series is generally good, particularly ($r \geq 0.9$) over the large expanses of African savanna and Australia where the overwhelming majority of BA on both “fire continents” occurs each year (Fig. 5). Less agreement is found in areas that are less fire-prone (e.g., Central Africa), in some cases to the point that r is essentially zero or even slightly negative, but for the most part these are limited to grid cells in which almost no BA is mapped in either product, and the time-series comparison for such cells effectively becomes an exercise in correlating noise. In practical terms, as well, these regions of poor agreement may not be a concern in many contexts since they contribute to only a very small fraction of the total global burned area (Fig. 8, inset).

4.2. Regional consistency

4.2.1. Regional spatial consistency

A limitation of the regression-based comparison (Fig. 6) is that the regression slope parameters are influenced by the large population of 0.25° grid cells with high burn proportions occurring in Africa and Australia (Fig. 5). To eliminate the effects of this bias, we partitioned the spatially explicit global annual BA totals into the 14 Global Fire Emissions Database (GFED) regions (Fig. S1 in Supplementary Material) that are defined based on fire behavior and seasonality (Giglio et al., 2006). The results are summarized in Table 2 and shown for a representative central year (2018) in Fig. 9 (exhaustive plots for each region and year from 2012 to 2013 are provided in supplementary Figs. S2–S15). Across regions, the mean annual BA discrepancy between VNP64A1 and MCD64A1 was smallest in Europe (0.1 % relative difference) and highest

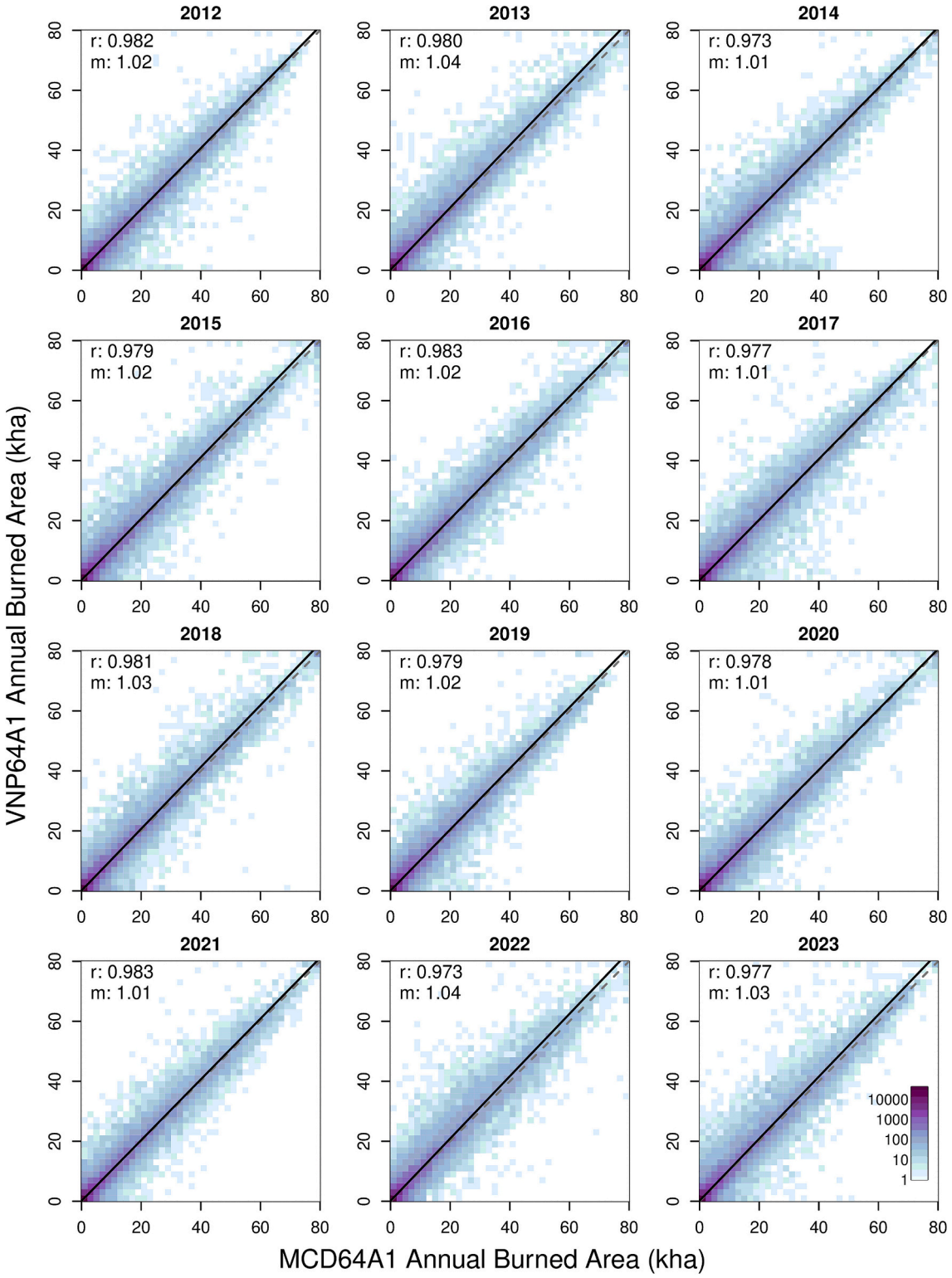

Fig. 6. Annual global spatial consistency between 0.25° gridded VNP64A1 versus MCD64A1 BA, defined by Pearson correlation (*r*) and orthogonal least-squares linear regression slope (*m*). The plot for 2012 depicts the 10-month period from March through December.

in Southeast Asia (33.1 % relative difference). The discrepancy was almost evenly split in direction, with a positive median relative difference of 10.7 % in eight regions (BONA, CEAM, EURO, MIDE, NHAF, SHAF, SEAS, and EQAS) and a negative median relative difference of −4.9 % in the remaining six regions (TENA, NHSA, SHSA, BOAS, CEAS, and AUST). Regression slopes varied somewhat, both regionally and annually, but generally remained reasonably close to unity (Table 2 and Figs. S2–S15). SHAF and NHAF are notable in that the regression slopes for these regions were exceptionally stable and near unity for all years (Figs. S9 and S10). As with the global analysis (Fig. 6), y-intercepts were included in the regression model but were found to be uniformly negligible.

We traced the singularly large surplus of VNP64A1 BA (relative to MCD64A1) in SEAS to a recurring pattern of differences in the fine-scale

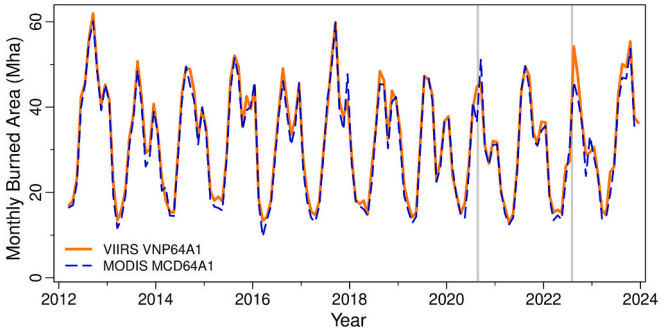

Fig. 7. Monthly total global burned area reported by the VNP64A1 and MCD64A1 BA products, from March 2012 through December 2023. The vertical grey bars indicate extended Aqua MODIS (2020) and S-NPP VIIRS (2022) outage periods. (For interpretation of the references to color in this figure legend, the reader is referred to the web version of this article.)

features and absolute numbers of VIIRS and MODIS active fire detections within a broad area covered by Myanmar, Thailand, Cambodia, and Vietnam. Within this region, VIIRS detects particularly large numbers of active fire pixels that have no proximate MODIS counterpart, and the VIIRS fire pixels in general are arranged in smaller clusters often only one or two 500-m grid cells in size after resampling onto the sinusoidal grid. In contrast, fire pixels from the two MODIS instruments are distributed over a much smaller number of larger clusters. A milder form of this pattern occurs intermittently in other regions, as expected given the smaller and growth-limited VIIRS footprint, but consistently recurs each year during the months of peak local fire activity in SEAS. This difference produces a comparative surplus of VIIRS BA associated with 1) slightly higher prior probabilities applied over a broader area of the mapped tile, and 2) an increase at many locations in the local cumulative conditional probability $F(n_B|B)$ that results in fewer grid cells tentatively classified as *burned* from being relabeled as *unburned* during the final algorithm relabeling phase.

4.2.2. Regional temporal consistency

Considering, as above, regional variations in the temporal consistency of the VNP64A1 and MCD64A1 products, Fig. 10 shows the respective monthly BA time series for each GFED region. In general, the time series exhibit reasonably good agreement in most regions, with very high correlation ($r \geq 0.995$) in Africa (NHAF and SHAF), Australia (AUST), and Southern Hemisphere South America (SHSA). The monthly time series in Boreal Asia (BOAS) and Southeast Asia (SEAS) were the least correlated, with correlation coefficients of 0.878 and 0.972, respectively. For BOAS this inconsistency was driven by a spuriously high MCD64A1 BA for March 2014 (7.24 Mha) that occurred in southeast Russia (tile h25v03) due to spectral confusion with rapid and extensive snow melt during the third week of March, shortly before true burning occurred in small, isolated patches less than a week later. It is well established that snow melt can spectrally resemble burning (Roy et al., 2005; Chuvieco et al., 2008). However, the corresponding March 2014 VNP64A1 product did not have this issue because the VIIRS cloud mask flagged a larger proportion of the daily surface reflectance observations as cloudy. The concomitant reduction in valid daily VIIRS observations softened the drop in SWIR surface reflectance associated with snow melt (which was more abrupt in the MODIS time series), to the extent that for VIIRS the change was not confused with burning. Excluding March 2014 from the BOAS time series increased the correlation to 0.978.

In SEAS, the lower correlation ($r = 0.972$) between the monthly VNP64A1/MCD64A1 time series was largely driven by slight differences in the reported dates of widespread cropland-residue burning in northwest India each year during October and November (Hall et al., 2024). Here, MCD64A1 tends to map more burned area than VNP64A1 during the last week of October, and less burned area than VNP64A1 product during the first week of November. This comparatively minor difference in timing is exaggerated by the monthly temporal bins used in our

Table 2
Regional 2013–2023 VNP64A1 and MCD64A1 mean annual burned area, relative VNP64A1-MCD64A1 BA difference with respect to MCD64A1 (Δ), and medians of the annual 0.25° regression slopes and Pearson correlation coefficients (*r*).

	Mean Annual Burned Area (Mha)				
Region	VNP64A1	MCD64A1	Δ	median slope	median *r*
BONA	3.9	3.5	10.0 %	1.07	0.974
TENA	2.9	3.0	−4.1 %	0.98	0.958
CEAM	2.8	2.5	13.4 %	1.02	0.924
NHSA	5.4	5.4	−0.5 %	0.89	0.943
SHSA	22.6	24.6	−8.3 %	0.95	0.976
EURO	0.7	0.7	0.1 %	1.02	0.916
MIDE	1.8	1.6	14.6 %	1.13	0.955
NHAF	113.5	108.1	5.0 %	0.99	0.981
SHAF	148.7	138.9	7.0 %	1.02	0.983
BOAS	8.2	8.6	−4.4 %	1.04	0.894
CEAS	11.8	12.6	−6.4 %	0.93	0.872
SEAS	18.6	14.0	33.1 %	1.27	0.932
EQAS	1.3	1.2	11.4 %	1.02	0.885
AUST	36.5	38.5	−5.3 %	0.98	0.989

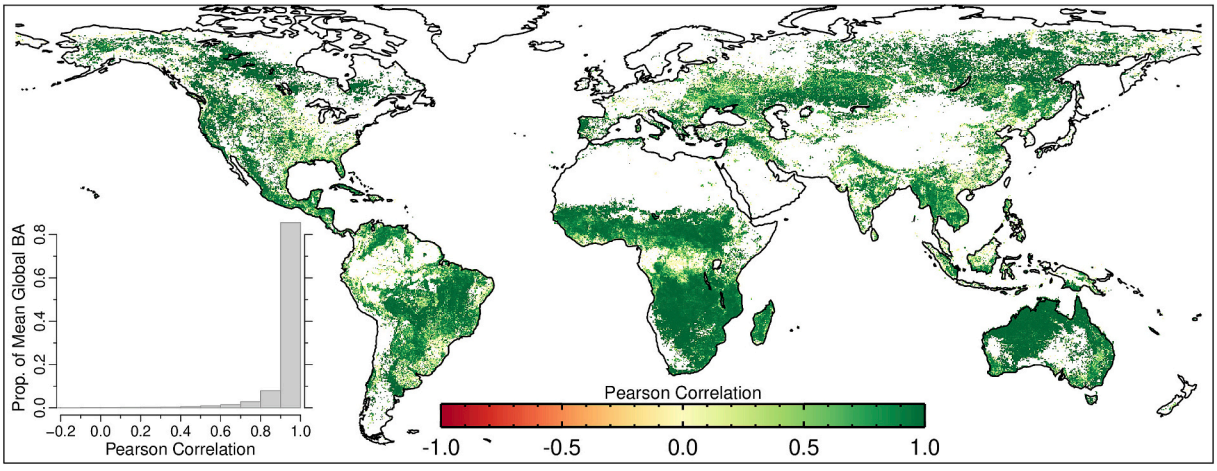

Fig. 8. Pearson correlation coefficient (*r*) of the VNP64A1/MCD64A1 0.25° gridded monthly BA time series from March 2012 through December 2023. Inset (lower left): Histogram of proportion of mean monthly global VNP64A1 BA contained within quantized correlation bins of width 0.1.

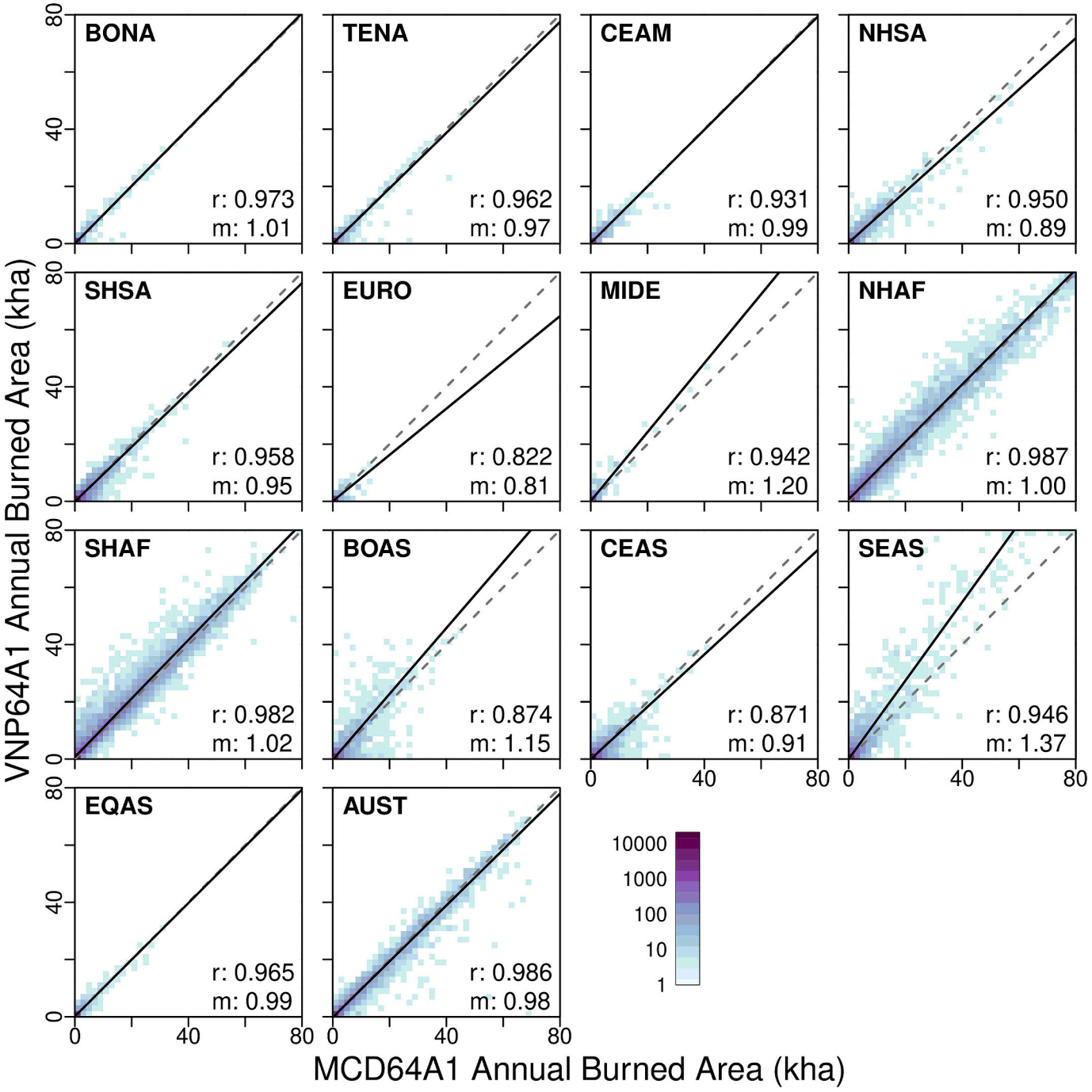

Fig. 9. Regional spatial consistency between 0.25° gridded VNP64A1 versus MCD64A1 BA for the year 2018. Shown for each plot is the Pearson correlation (r) and orthogonal least-squares linear regression slope (m).

analysis. Excluding the October and November monthly totals from the SEAS time series raised the correlation coefficient to $r = 0.983$, which is a noticeable improvement in temporal consistency but does not capture the noticeable difference in the magnitudes of the BA time series in this region.

4.3. Fine-scale burn-date consistency

A monthly time step is appropriate for the broad-scale assessments described above but is too coarse to resolve smaller temporal discrepancies between the estimated burn dates provided by the VNP64A1 and MCD64A1 BA products. To more precisely assess the consistency of these dates we compared the 500-m VNP64A1 and MCD64A1 products at their native resolution. Each year from 2012 through 2023 was analyzed separately so that variations in product temporal consistency over time could be detected. The analysis was conducted by calculating the difference Δt_B in the estimated burn date for each 500-m grid cell reported as burned in both products during a given month, tallying each value to generate regional Δt_B frequency histograms on an annual basis. Fig. 11 shows the resulting burn-date reporting distributions for each GFED region. For all regions and all years, the median difference in reported burn date was 0 days, indicating no temporal bias between the products. Across regions, the discrepancy in burn date was lowest in AUST, where the mean interquartile range (IQR) over all years was 1.2

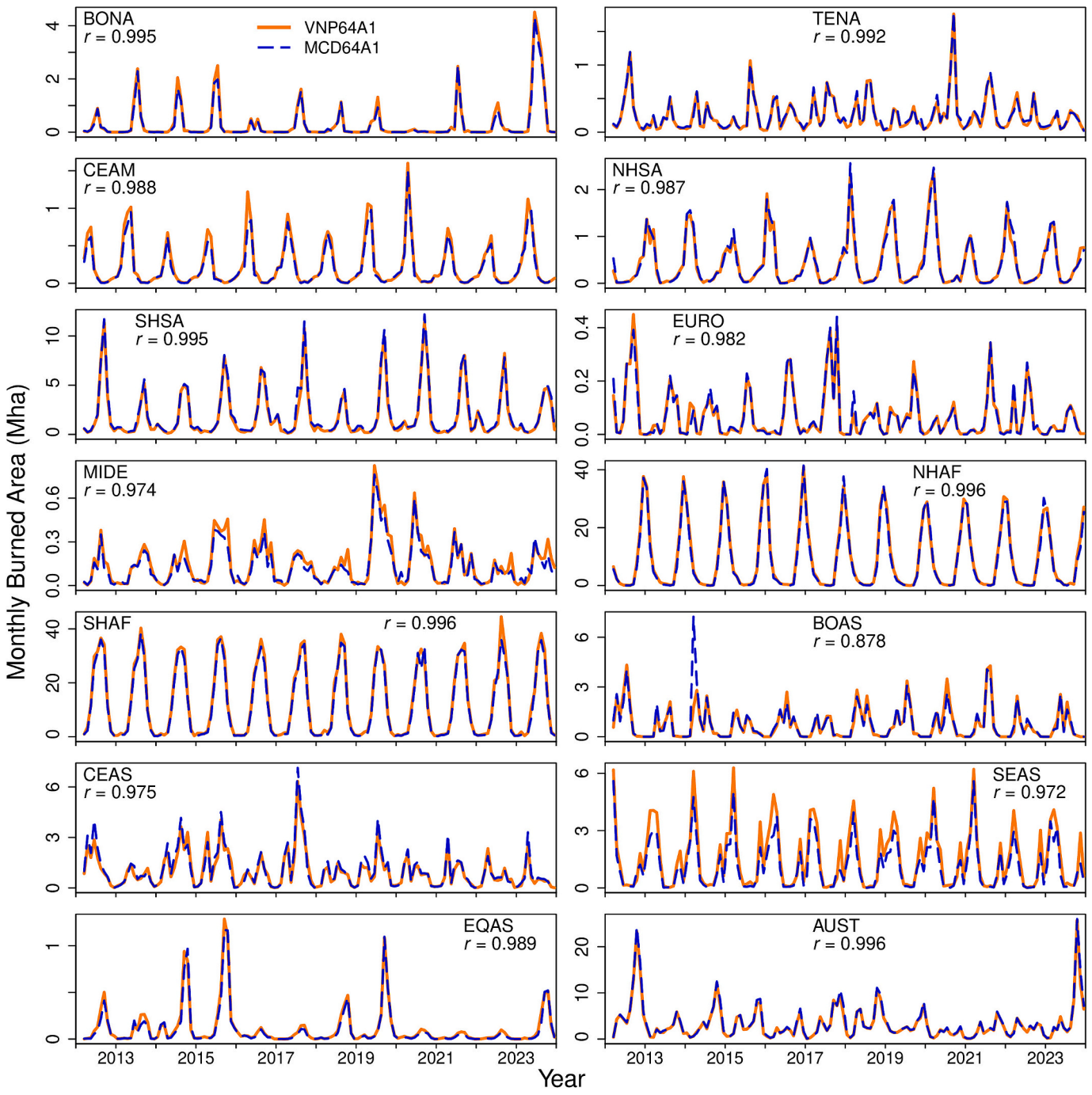

Fig. 10. Monthly total global burned area reported by the VNP64A1 and MCD64A1 BA products, from March 2012 through December 2023 for the 14 GFED regions, with respective Pearson correlation coefficients (*r*).

days, and highest in EQAS (Equatorial Asia), where the mean IQR over all years was 4.8 days (Fig. S16 in Supplementary Material). Much of this regional variation is attributable to the lack of morning/early-evening VIIRS observations that can compensate for cloud-obscured VIIRS observations acquired in the afternoon and late evening, and notably the EQAS GFED region is well established to be particularly cloud-prone (Vignesh et al., 2020), including at the times of the Terra and Aqua MODIS overpass (Roy et al., 2006; King et al., 2013). Globally, the mean IQR was 1.75 days, driven overwhelmingly by the preponderance of BA in Africa (i.e., in NHAF and SHAF).

5. Global validation

5.1. Areal uncertainty

5.1.1. Methodology

The VNP64 product was validated following the same design-based inference methodology and using the same independent reference dataset used to assess the accuracy of the Collection 6 (C6) MCD64A1 product (Boschetti et al., 2019). To provide a meaningful baseline, we also present the validation results of the most recent C6.1 MODIS MCD64A1 product. In this section the validation methodology is briefly summarized for completeness. For an exhaustive description of the independent reference data sampling methodology, we refer to Boschetti

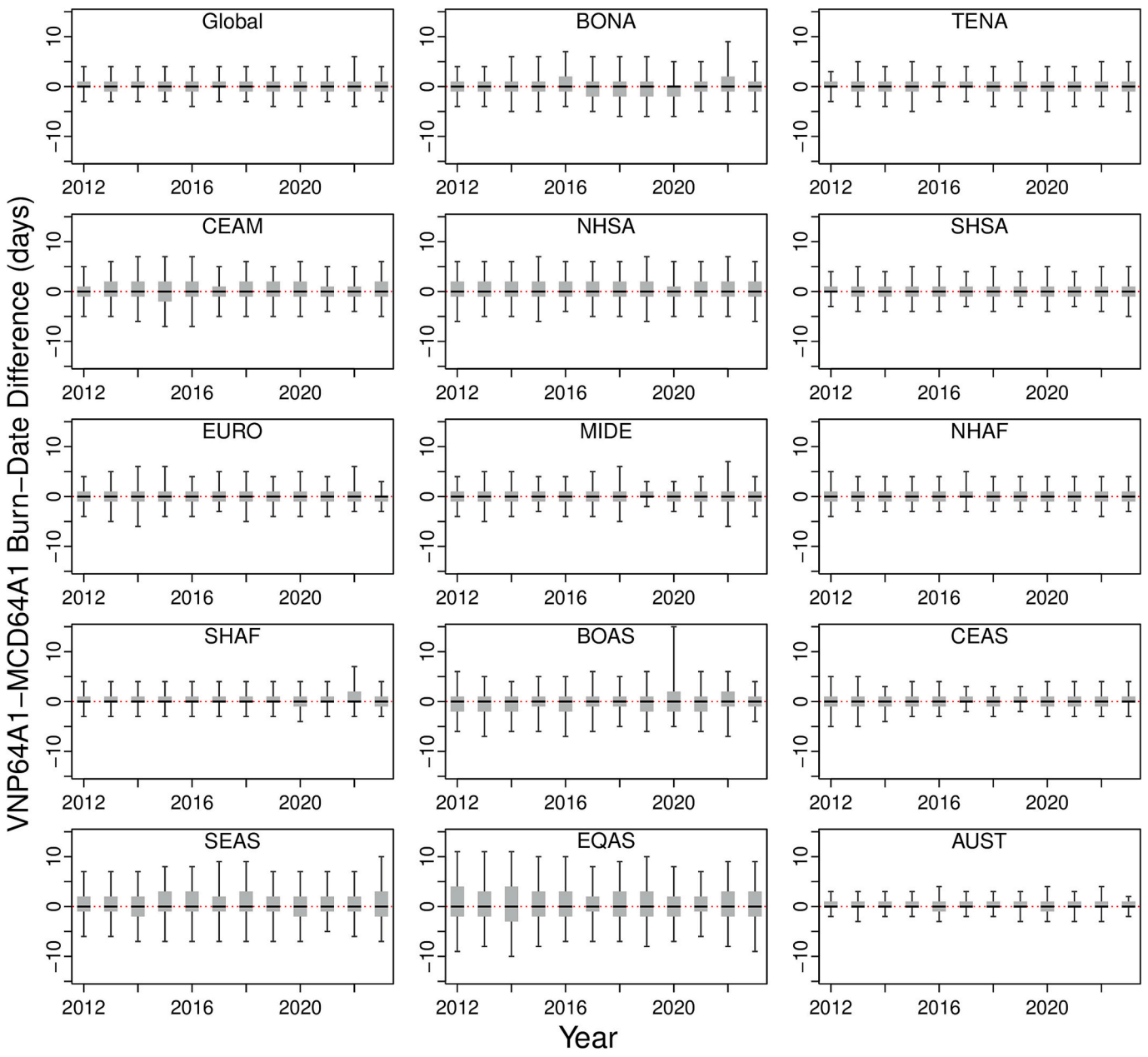

Fig. 11. Regional box and whisker plots summarizing on an annual basis the differences in VNP64A1 and MCD64A1 reported burn dates for all 500-m grid cells reported as burned in both monthly products. The horizontal black bars indicate the median difference in burn date, the grey bars span the 25th through 75th percentiles of the difference in burn date, and the whiskers indicate the 5th and 95th percentiles of the difference in the burn date. Negative differences indicate that the VNP64A1 reported burn date precedes that of MCD64A1.

et al. (2016). For a description of the independent reference-data mapping protocol and the accuracy metrics and standard error estimators, we refer to Boschetti et al. (2019).

The validation was conducted by comparing the coarse-resolution (VIIRS and MODIS) BA maps with an independent reference dataset consisting of visually interpreted 30-m Landsat 8 Operational Land Imager (OLI) image pairs, acquired 16 days apart. These independent reference data were selected using a stratified random sampling approach, that allows for probability sampling of Landsat data in both time and space. To sample the globe in the spatial domain with non-overlapping sampling units, the Thiessen Scene Area (TSA) tessellation of the Landsat path/row geometry was used. The TSA grid was combined in time with the 16-day Landsat acquisition calendar to provide a sampling grid of three-dimensional elements (voxels). The grid of voxels was stratified spatially into seven aggregated biomes derived from the Olson global ecoregion map (Olson et al., 2001). The voxels in each biome were stratified temporally by taking into account the timing of the MODIS MOD14 (Terra) and MYD14 (Aqua) active fire detections. Voxels were assigned to a 'high fire activity' stratum if there were more active fire detections than a biome-specific threshold, and the remainder were assigned to a 'low fire activity' stratum. As a result, the three-dimensional voxel grid was defined by 14 strata (i.e., seven biomes, each with two fire activity levels). The voxel grid defined by the WRS tessellation and Landsat 8 acquisition calendar, supports probability sampling in both the temporal and spatial domains, and constitutes a straightforward and rigorous framework for the validation of global burned area products, which are variable in time and space.

A total of 561 Landsat 8 OLI image pairs (1122 images), acquired between 1 March 2014 and 19 March 2015, were randomly selected with approximately equal allocation among the 14 strata and then

visually interpreted. A total of 558 Landsat 8 OLI image pairs were interpreted and used in Boschetti et al. (2019); for this study the dataset was augmented with three additional image pairs from the same random extraction that could not be originally used due to a rare Landsat geolocation metadata issue.

This stratified random sampling strategy satisfies the Stage 3 requirements defined by the Committee on Earth Observation Satellites (CEOS) Land Product Validation subgroup, that "*product accuracy has been assessed, and the uncertainties in the product established via independent measurements made in a statistically robust way, at multiple locations and time periods that represent the full range of conditions present in the product, and is characterized by the selection of independent reference data via probability sampling*" (Morisette et al., 2006). Importantly, any probability sampling approach implies that the probability of each individual population element being included in the sample (i.e. the *inclusion probability*) is unambiguously defined and can be used for unbiased estimation of accuracy metrics and associated standard errors (Boschetti et al., 2016).

5.1.2. Estimated confusion matrices and confusion matrix-based accuracy metrics results

A confusion matrix was computed at 30-m resolution for each Landsat 8 interpreted image pair and the contemporaneous VNP64A1 product. These individual confusion matrices were combined to estimate per-biome and global confusion matrices (Table 3) by taking into account the inclusion probability of each Landsat 8 image pair (supplementary Table S1). The areal accuracy of the products was characterized at the 30-m resolution of the Landsat independent reference data using standard accuracy metrics derived from global and from biome-specific confusion matrices, i.e., the estimated overall accuracy ($\widehat{OA}$), BA omission error ratio ($\widehat{OE}$), BA commission error ratio ($\widehat{CE}$), and relative bias ($\widehat{relB}$), reported in Table 4 together with the associated estimated standard errors, denoted $\widehat{SE}$ (see Boschetti et al., 2019, Section 2.3.1.2).

The VNP64A1 product $\widehat{OA}$ is high both globally (99.7 %) and in each biome (>99 %), reflecting the generally low prevalence of burned areas, which in every biome occur in only a small proportion of the landscape. This is expected due to the small proportion (approximately 2.6 %) of the global land area that burned from 2012 to 2023 (Section 4.1). Globally, the $\widehat{OE}$ is 72.4 % and the $\widehat{CE}$ is 36.7 %, with the prevalence of omission errors reflected by a $\widehat{relB}$ of −56.5 %. While these errors appear high, they reflect the 500-m VNP64A1 product accuracy relative to the 30-m resolution reference data. The confusion matrix accuracy metrics are complemented by regression metrics computed on BA proportions in coarse resolution cells (Section 5.3) to evaluate the product accuracy and precision at the coarse resolution scale used for climate and emission models (Boschetti et al., 2003; Boschetti et al., 2006; Tansey et al., 2008; Roy and Boschetti, 2009). The regression analysis indicates whether any of the omission and commission errors observed at 30-m resolution compensate at relatively local scale, due to factors including the presence of mixed 500-m cells (Boschetti et al., 2004), degradation of the data resolution due to resampling of the orbital swath data to 500-m sinusoidal-projection pixels (Wolfe et al., 1998; Campagnolo et al., 2016), and temporal discrepancies between the VIIRS data and the reference data (Boschetti et al., 2019; Franquesa et al., 2022).

Table 3
Global and per-biome confusion matrices for the VNP64A1 product, reported in terms of area [km^2], and constructed so that the rows represent the VNP64A1 product, and the columns represent the independent Landsat-8 burned area reference data. The diagonal elements of the confusion matrix ($\widehat{A}_{11}$ and $\widehat{A}_{22}$) correspond to the area correctly mapped by the VNP64A1 product as burned and unburned, respectively, and the off-diagonal elements ($\widehat{A}_{12}$ and $\widehat{A}_{21}$) correspond to the area incorrectly mapped as burned and unburned respectively.

Biome	$\widehat{A}_{11}$ [km^2]	$\widehat{A}_{12}$ [km^2]	$\widehat{A}_{21}$ [km^2]	$\widehat{A}_{22}$ [km^2]
Tropical Forest	185,444	479,252	2,475,088	4.56×10^8
Temperate Forest	29,513	22,757	289,177	3.32×10^8
Boreal Forest	108,763	30,045	38,186	3.85×10^8
Tropical Savanna	1,609,031	635,217	2,339,571	4.16×10^8
Temperate Savanna	145,635	32,729	222,240	2.88×10^8
Mediterranean	7082	10,938	117,161	0.63×10^8
Deserts/Xeric Shrublands	27,481	11,806	70,173	5.52×10^8
Global	2,112,950	1,222,745	5,551,595	2.49×10^9

The accuracy metric values (Table 4) are variable among the biomes, with the lowest $\widehat{OE}$ in Boreal Forest (26.0 %) and the lowest $\widehat{CE}$ in Temperate Savanna (18.3 %) and Boreal Forest (21.6 %), and the highest errors in the Tropical Forest, Temperate Forest, and Mediterranean biomes ($\widehat{OE}$> 90 %, $\widehat{CE}$ > 40 %). The $\widehat{relB}$ values are negative in all biomes, and range from −5.5 % in Boreal Forest, to −85.5 % in Mediterranean. Globally, the standard errors of the four accuracy metrics are less than 6 %, with $\widehat{SE}(\widehat{OA}) < 0.1\%$, $\widehat{SE}(\widehat{OE}) = 4.4\%$, $\widehat{SE}(\widehat{CE}) = 3.1\%$, and $\widehat{SE}(\widehat{relB}) = 5.3\%$. At the biome level, all standard errors are <15 %.

Comparison of the VNP64A1 accuracy metrics with those of the C6.1 MCD64A1 product (Tables 5, 6) indicates that globally the two products have substantially identical accuracy. The two products have the same $\widehat{OA}$, whereas VNP64A1 has slightly higher $\widehat{OE}$ and $\widehat{CE}$ than MCD64A1, but both differences ($\widehat{OE}$ 72.4 % vs 71.5 %, $\widehat{CE}$ 36.7 % vs. 35.2 % for VNP64A1 and MCD64A1 respectively) are within the standard errors of the VNP64A1 estimates ($\widehat{SE}(\widehat{OE})$ 4.4 %, $\widehat{SE}(\widehat{CE})$ 3.1 %) and accordingly the relative biases are also nearly identical (−56.5 % and −56.7 % for VNP61A1 and MCD64A1, respectively). At the biome level, the differences between the product accuracy metrics are small (< 6 %), with the only exception of $\widehat{CE}$ in Tropical Forest (VNP64A1: 72.1 %, MCD64A1: 60.1 %) and Temperate Forest (VNP64A1: 43.5 %, MCD64A1: 51.7 %), and $\widehat{relB}$ in Deserts and Xeric Shrublands (VNP64A1: -59.8 %, MCD64A1: −53.7 %). When considering the standard errors of the estimates, those differences are however well within the 95 % confidence interval (i.e., within 1.96 SE of the estimates).

5.1.3. Coarse resolution regression metric results

The error matrix and derived accuracy metrics were complemented by coarse resolution regression metrics, based on the comparison of the proportion of 5-km × 5-km cells detected as burned by VNP64A1 with the proportion mapped as burned in the Landsat 30-m independent reference data (see Boschetti et al., 2019, Section 2.3.2). Following the methods presented in Boschetti et al. (2006), the slope and intercept of the regression line were estimated through a weighted least squares procedure, where the weights are the inverse of the inclusion probabilities (Table S1); the same weights were also used to estimate the coefficient of determination (r^2) and root mean square error (RMSE). For a comprehensive justification for the use of the inverse of the inclusion probabilities as estimation weights, see Lohr (2022). Figs. 12 and 13 present the scatterplots and weighted linear regression metrics, per-biome and globally, for the VNP64A1 and MCD64A1 products, respectively.

Globally, the high correlation ($r^2 = 0.70$), the slope close to unity (0.83), and the small negative intercept (−0.0006) indicate that the errors of omission and commission significantly compensate at relatively local scales. High correlation ($r^2 > 0.75$) and slopes close to unity (0.85 to 1.12) are observed in Boreal Forest, Tropical Savanna and Temperate Savanna, whereas low correlation ($r^2 < 0.5$) and slopes significantly below unity (0.08 to 0.57) are observed in the other four biomes.

Consistent with the confusion matrix results (Section 5.2), the regression metrics are very similar to those of the C6.1 MCD64A1 product (Fig. 13). Globally, the two products have identical correlation

Table 4
Estimated global and per-biome accuracy metrics, and associated standard errors, for the VNP64A1 product derived from the Table 3 estimated confusion matrices.

Biome	$\widehat{OA}$	$\widehat{SE}(\widehat{OA})$	$\widehat{OE}$	$\widehat{SE}(\widehat{OE})$	$\widehat{CE}$	$\widehat{SE}(\widehat{CE})$	$\widehat{relB}$	$\widehat{SE}(\widehat{relB})$
Tropical Forest	99.4 %	0.4 %	93.0 %	1.6 %	72.1 %	12.3 %	−75.0 %	7.7 %
Temperate Forest	99.9 %	0.1 %	90.7 %	4.7 %	43.5 %	11.8 %	−83.6 %	5.7 %
Boreal Forest	> 99.9 %	0.1 %	26.0 %	6.2 %	21.6 %	2.8 %	−5.5 %	6.0 %
Tropical Savanna	99.3 %	0.1 %	59.3 %	6.1 %	28.3 %	2.5 %	−43.2 %	7.3 %
Temperate Savanna	99.9 %	0.0 %	60.4 %	11.1 %	18.3 %	4.7 %	−51.5 %	11.1 %
Mediterranean	99.8 %	0.1 %	94.3 %	7.7 %	60.7 %	13.0 %	−85.5 %	14.9 %
Deserts/Xeric Shrublands	> 99.9 %	<0.1 %	71.9 %	4.5 %	30.1 %	5.4 %	−59.8 %	5.6 %
Global	99.7 %	<0.1 %	72.4 %	4.4 %	36.7 %	3.1 %	−56.5 %	5.4 %

Table 5
Global and per-biome confusion matrices for the MCD64A1 product. See Table 3 caption for details.

Biome	$\widehat{A}_{11}$ [km^2]	$\widehat{A}_{12}$ [km^2]	$\widehat{A}_{21}$ [km^2]	$\widehat{A}_{22}$ [km^2]
Tropical Forest	254,923	384,414	2,394,935	4.56×10^8
Temperate Forest	17,184	18,395	301,321	3.32×10^8
Boreal Forest	100,701	30,584	37,236	3.85×10^8
Tropical Savanna	1,618,372	640,139	2,330,464	4.16×10^8
Temperate Savanna	145,911	35,409	222,328	2.88×10^8
Mediterranean	6681	9812	117,554	0.63×10^8
Deserts/Xeric Shrublands	32,686	12,617	65,057	5.52×10^8
Global	2,176,458	1,131,370	5,468,896	2.49×10^9

coefficients, and very similar slope and intercept terms. At the biome level, the most significant differences are the slightly better performance of VNP64A1 in the Temperate Forest and Temperate Savanna biomes, with higher correlation and slope equally near or closer to unity than MCD64A1, whereas in the Boreal Forest biome the slope is further from unity (VNP64A1: 1.12, MCD64A1: 1.02) but has a higher coefficient of determination (VNP64A1: 0.76, MCD64A1: 0.73). In all other biomes, the VNP64A1 performance is slightly worse than MCD64A1.

5.2. Temporal uncertainty

We repeated the temporal reporting uncertainty assessment undertaken for the C6 MODIS BA product (Boschetti et al., 2010) for both the C2 VNP64A1 and C6.1 MCD64A1 products (Fig. 14). The assessment, which here was undertaken using 2023 product data, examines the temporal difference between the date of MODIS Terra and Aqua active fire detections and the spatially coincident VNP64A1/MCD64A1 mapped date of burning within a 90-day buffer. Note that while MODIS active fire data are used in the MCD64A1 mapping algorithm, they are not used to estimate the date of burning, which is determined by examination of the surface reflectance time series. Thus, in the context of this temporal assessment, MODIS active fire data can be considered reasonably independent. MODIS offers the additional benefit of providing both morning and afternoon overpasses that together yield a less-aliased temporal sample of fire activity than is provided by VIIRS or Sentinel-3.

Globally, 38 % of the VNP64A1 burned pixels had burn dates that matched the date of an active fire, versus 46 % for MCD64A1. For burn dates within 2 days of an active fire, the proportions were significantly higher and essentially identical (71 % for VNP64A1 versus 72 % for MCD64A1). These differences are consistent with the fine-scale intercomparison of VNP64A1 and MCD64A1 burn dates (Section 4.3), where globally 50 % (i.e., the proportion within the IQR) of absolute burn-date differences were $\leq$ 1.75 days. We attribute the somewhat lower burn date temporal reporting accuracy of the VIIRS product primarily to the lack of morning/early-evening VIIRS observations (i.e., matching the Terra MODIS) that can compensate for cloud-obscured afternoon/late-evening VIIRS observations.

6. Discussion

We have described the NASA C2 VIIRS burned area product (VNP64A1), which is intended to continue the 25-year global burned area record provided by its MODIS MCD64A1 predecessor beyond the imminent decommissioning of NASA's Terra and Aqua satellites. The VNP64A1 product is derived using an adaptation of the C6.1 MCD64A1 algorithm and employs, for compatibility, the same grid and 500-m reporting resolution used for MCD64A1. The algorithm adaptation was ultimately limited to three comparatively minor changes, in part because no combination of parameter adjustments could, nor was expected to, fully compensate for the many differences between the VIIRS and MODIS sensors and the spatiotemporal sampling of their respective observations. Future work will focus on generic algorithm refinements, such as sharing training samples between adjacent tiles, and exploiting observations from multiple VIIRS sensors to better suppress VIIRS BRDF effects (Section 3.3).

The key rationale for developing the VIIRS-based VNP64A1 product is to continue the existing long-term MODIS BA record, which is now nearly 25 years in duration, into the post-MODIS S-NPP and JPSS era, facilitating the development of a consistent multi-sensor burned area climate data record suitable for long-term monitoring and research. A consistency assessment conducted via intercomparison of the VPN64A1 and MCD64A1 products for 2012–2023 was therefore an essential component of this work. This assessment revealed that, globally, the VNP64A1 product consistently mapped slightly more BA each year than the MCD64A1 product, with the relative surplus ranging from 2.1 % in 2017 to as much as 6.3 % in 2013.

Regional VNP64A1 and MCD64A1 product consistency was more variable, with mean annual BA discrepancies ranging in magnitude from 0.1 % (Europe) to 33.1 % (Southeast Asia) and split in direction across

Table 6
Estimated global and per-biome accuracy metrics, and associated standard errors, for the MCD64A1 product derived from the Table 5 estimated confusion matrices.

Biome	$\widehat{OA}$	$\widehat{SE}(\widehat{OA})$	$\widehat{OE}$	$\widehat{SE}(\widehat{OE})$	$\widehat{CE}$	$\widehat{SE}(\widehat{CE})$	$\widehat{relB}$	$\widehat{SE}(\widehat{relB})$
Tropical Forest	99.4 %	0.4 %	90.4 %	1.4 %	60.1 %	7.0 %	−75.9 %	7.1 %
Temperate Forest	99.9 %	0.1 %	94.6 %	2.0 %	51.7 %	8.1 %	−88.8 %	6.1 %
Boreal Forest	> 99.9 %	0.1 %	27.0 %	10.7 %	23.3 %	3.1 %	−4.8 %	11.3 %
Tropical Savanna	99.3 %	0.1 %	59.0 %	6.2 %	28.3 %	2.7 %	−42.8 %	8.3 %
Temperate Savanna	99.9 %	< 0.1 %	60.4 %	11.3 %	19.5 %	5.0 %	−50.8 %	10.5 %
Mediterranean	99.8 %	0.1 %	94.6 %	7.2 %	59.5 %	12.3 %	−86.7 %	19.1 %
Deserts/Xeric Shrublands	> 99.9 %	< 0.1 %	66.6 %	5.7 %	27.9 %	5.3 %	−53.7 %	8.1 %
Global	99.7 %	< 0.1 %	71.5 %	4.3 %	34.2 %	2.5 %	−56.7 %	5.0 %

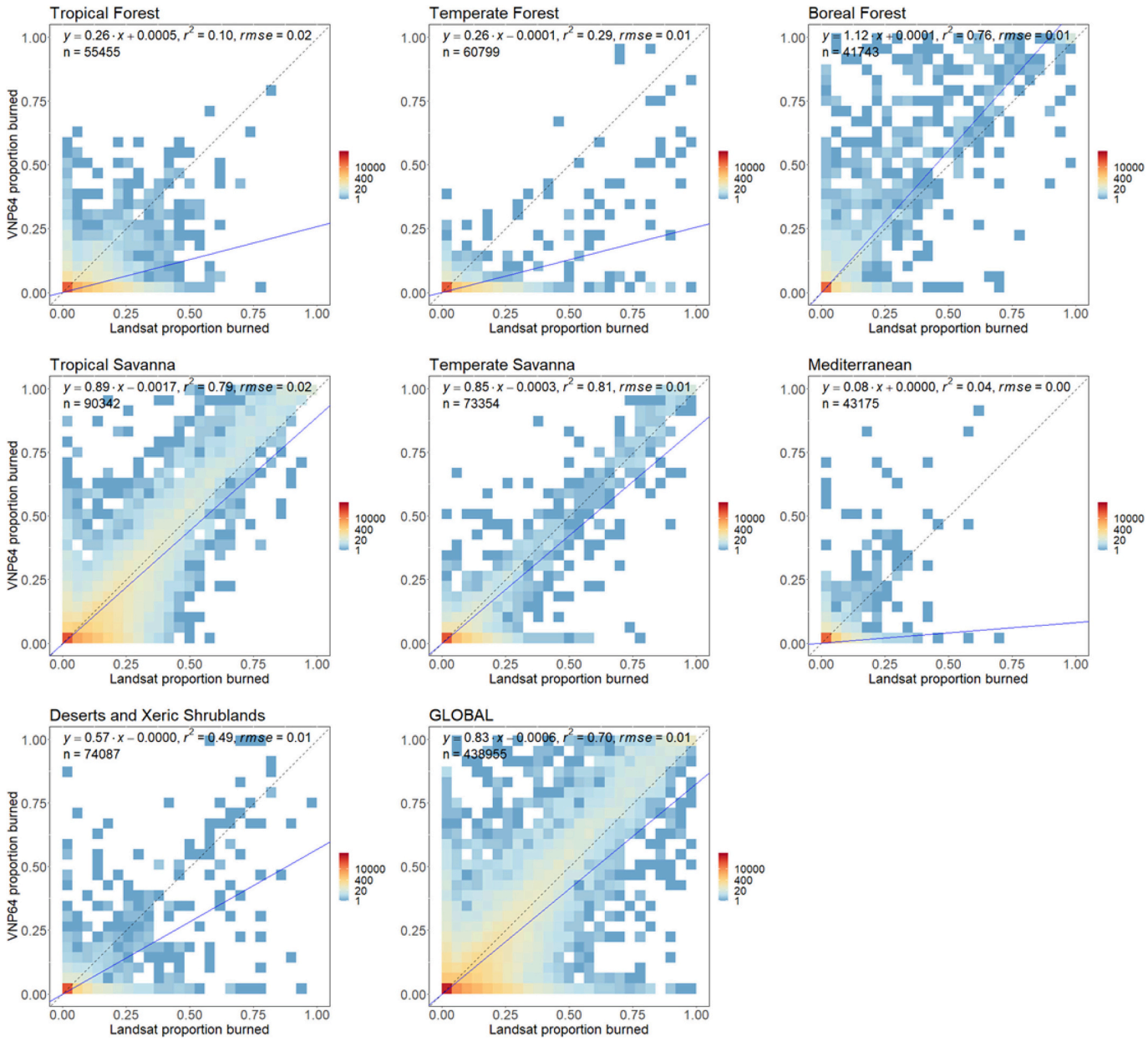

Fig. 12. Scatter plot of the proportions of coarse resolution 5-km × 5-km cells labeled as burned by the VNP64A1 product, plotted against the proportion labeled as burned by the Landsat 8 independent reference dataset, for each biome and globally. The point density distribution is calculated using a 25 × 25 quantization of the plot axes and is displayed with a logarithmic color scale. The blue lines show the weighted least square regression of the proportion data; the dashed 1:1 lines are shown as reference. (For interpretation of the references to color in this figure legend, the reader is referred to the web version of this article.)

eight regions (median: +10.7 %) and the remaining six (median: −4.9 %). Future work directed toward identifying and mitigating the uniquely challenging feature(s) that limit product consistency in Southeast Asia is required. While we identified differences in the VIIRS and MODIS active fire observations as the primary driver of the lower product consistency in this region, additional factors are likely also at play.

Monthly temporal product consistency was more uniformly high, with the singularly low exception in Boreal Asia ($r = 0.878$) being caused by a single month of spuriously high MCD64A1 BA in March 2014. At the daily temporal scale, the uniform absence of a systematic temporal reporting bias between the VNP64A1 and MCD64A1 products across all regions and years (Section 4.3) is extremely encouraging. However, the random temporal differences that can occur over short periods (e.g., days) must be recognized since the temporal-discrepancy frequency distributions (Fig. 11) are considerably broader in some regions. Considering the worst-case example of EQAS, where the mean IQR of the differences in burn dates was 4.8 days, the product burned area maps for a specific single day would likely look very different.

Stage-3 validation of the VNP64A1 and MCD64A1 BA products revealed very similar error metrics globally and with very few exceptions also across seven validation biomes at the scale of the 30-m Landsat imagery. This finding again indicates a high level of spatial product consistency. Coarse resolution BA products are (appropriately) rarely used at the extremely stringent scale of the Landsat-based validation, and in this context the coarse-resolution regression validation results usefully indicate that, for both products, the errors of omission and commission significantly and nearly identically compensate at relatively local scales (such as a 0.25° grid cell or a GFED region) that are many orders of magnitude larger than a 30-m pixel.

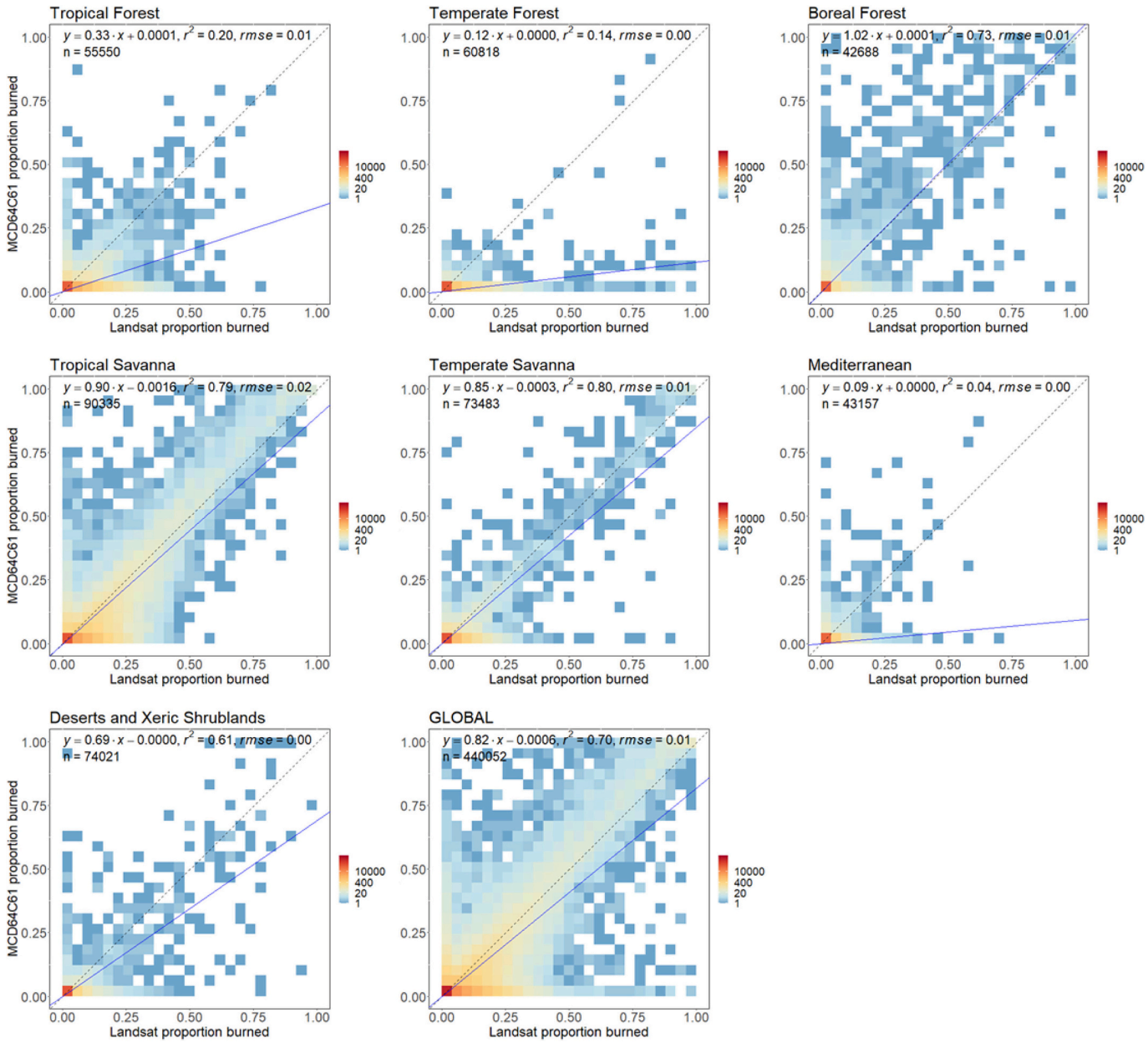

Fig. 13. Same as Fig. 12, for the MCD64A1 product.

The VNP64A1 product performance (accuracy and consistency in space and time) may be improved by using observations from multiple VIIRS sensors in the BA mapping algorithm. The planned series of VIIRS satellite platforms (currently S-NPP, NOAA-20, and NOAA-21) have Aqua-compatible local equator crossing times of 1:30/13:30. While this may seem redundant given the full daily global coverage provided by VIIRS, the different orbital phasing of these platforms results in an increased number of available near-nadir observations when combined. For example, the S-NPP and NOAA-20 satellites are out of phase by one-half orbit relative to each other, and combined provide significantly more near-nadir observations of a location than a single sensor (Lin et al., 2022). We found through testing that using S-NPP and NOAA-20 VIIRS data in combination improved the spatial fidelity of the monthly temporal composites employed in the mapping algorithm, with a 10 %–20 % average reduction (depending on latitude) in the areal footprint of the swath pixels from which the composites were constructed. The higher fidelity of the temporal composites is in turn expected to reduce the minimum detectable burned patch size. However, operating in this combined mode was not possible for C2 due to the heavy burden placed on NASA's VIIRS land processing system but is planned for a forthcoming Collection 3 reprocessing. Similarly, incorporation of active fire detections from the ESA Sentinel-3 Sea and Land Surface Temperature Radiometer (SLSTR; Xu and Wooster, 2023) is being explored to provide morning-overpass active fire observations. These additions – a second VIIRS sensor plus morning fire observations – are expected to improve the spatial and temporal consistency of the MODIS and VIIRS BA data records, though they would not provide morning/early-evening *surface reflectance* observations that can compensate for cloud-obscured afternoon/late-evening VIIRS observations (Section 5.2). The incorporation of SLSTR surface reflectance imagery into the VIIRS processing chain is more challenging due to spectral and scan-related differences between the sensors, however similar exploratory efforts are underway and may eventually prove fruitful. We note lastly that the computationally less-expensive tactic of generating a separate Aqua-only version of the MCD64A1 product (i.e., "MYD64A1") as a means of improving VNP64A1/MCD64A1 consistency is not viable since the resulting single-

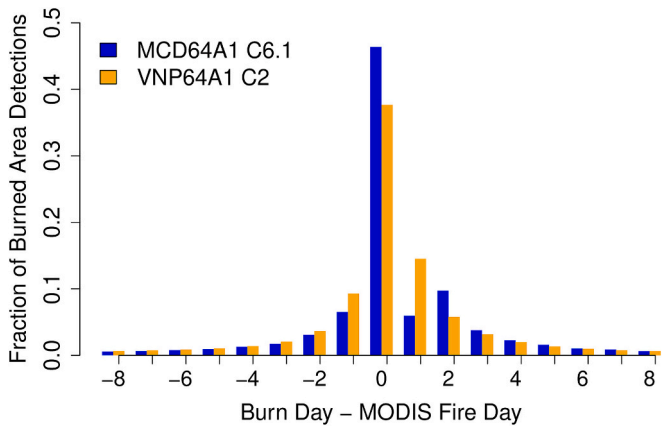

Fig. 14. Histogram of time differences (in days) between spatially coincident MODIS MCD64A1 and VIIRS VNP64A1 burned area and MODIS active fire detections for all land tiles during 2023. Negative differences indicate that the MODIS active fire detection precedes the burned area detection. A total of ~9.2 million 500-m grid cells were considered.

MODIS product suffers in too many respects from the loss of usable input data.

Given the importance for wildfire monitoring, the need for global fire product continuity into the VIIRS era is paramount. A systematically derived, long-term, global BA record is needed to contextualize, model, and predict changes in fire activity, particularly under a changing climate, and the VIIRS BA product represents a major step toward achieving continuity with the long-term MODIS BA data record. Due to the MODIS-VIIRS sensor differences, and lack of a morning VIIRS overpass, the C2 VIIRS and C6.1 MODIS burned area products are not identical, and reporting discrepancies between them become more evident at finer resolutions. Simple concatenation of the MCD64A1 and VNP61A1 BA time series at local scales is not advisable for long-term trend analyses but may be acceptable at the broad scales of some GFED regions (e.g., EURO, NHSA) provided the potential impact(s) of the known product discrepancies on the analysis are considered, particularly in the interpretation of results. Looking forward, the inter-comparison and validation results reported here show that the two products closely match in time and space and have very similar accuracy, thus indicating that a single harmonized long-term burned area record could be successfully generated at local scales through their statistical inter-calibration.

7. Conclusions

We have described the NASA Collection 2 VIIRS burned area product (VNP64A1), which is intended to continue the 25-year global burned area record provided by its MODIS predecessor (MCD64A1) beyond the imminent decommissioning of NASA's Terra and Aqua satellites. The VNP64A1 product is derived using a slightly modified adaptation of the Collection 6.1 MCD64A1 algorithm and employs, for compatibility, the same grid and 500-m reporting resolution used for MCD64A1. The VNP64A1 product is publicly available, with global coverage from 2012 to present day, and will be produced systematically over the life of the NOAA/NASA JPSS mission into the 2030s.

To broadly assess the C2 VNP64A1 and C6.1 MCD64A1 product consistency, we compared the respective monthly series from March 2012 through December 2023. Globally, the VNP64A1 product consistently mapped slightly more BA each year than the MCD64A1 product, with the relative surplus ranging from 2.1 % in 2017 to as much as 6.3 % in 2013. Global consistency at the monthly scale was very high, with a Pearson correlation coefficient of 0.989 and a mean relative monthly discrepancy of 4.1 %. Regionally, the mean annual BA discrepancy between the products was smallest in Europe (0.1 % relative difference) and highest in Southeast Asia (33.1 % relative difference), with a median absolute relative difference of 6.7 % over all regions. Regional monthly temporal consistency was generally good, with the highest correlations ($r \geq 0.995$) in Africa, Australia, and Southern Hemisphere South America, and a singularly low correlation ($r = 0.878$) in Boreal Asia due to a malfunction associated with snow melt in the March 2014 MCD64A1 product. A fine-scale (500-m) assessment of differences in reported burned dates revealed no systematic temporal reporting bias between the products.

We validated both products to CEOS Stage 3 using independent burned area reference maps derived from Landsat 30-m imagery. Globally, the estimated VNP64A1-product BA commission and omission error ratios were 36.7 % and 72.4 %, respectively, and a relative bias of −56.5 %. The MCD64A1-product accuracy metrics were highly comparable (34.2 % commission error, 71.5 % omission error, −56.7 % relative bias) again indicating high consistency between the products. We note that while the VNP64A1 product detected on average 4.33 % more annual burned area than MCD64A1, the differences are within the reported estimated standard error of the relative biases. The VNP64A1 accuracy varied among the biomes, with the lowest omission error in Boreal Forest (26.0 %) and the lowest commission error in Temperate Savanna (18.3 %). The highest errors occurred in the Tropical Forest, Temperate Forest, and Mediterranean biomes, with omission and commission error ratios exceeding 90 % and 40 %, respectively. The relative bias was negative in all biomes, ranging from −5.5 % in Boreal Forest to −85.5 % in Mediterranean.

The 30-m-scale accuracy assessment was complemented by coarse-resolution regression in which the proportions of 5-km × 5-km cells detected as burned by VNP64A1/MCD64A1 were compared with the proportions mapped as burned in the independent Landsat reference data. Globally, the two products had the same correlation ($r^2 = 0.70$), nearly identical slope (0.83 VNP64A1, 0.82 MCD64A1) and identical intercept (~ −0.0006) regression terms, consistent with the confusion-matrix-based results.

Finally, using MODIS fire-detection dates as a reference, we assessed the temporal reporting accuracy of the two products and found that, globally, 38 % of the VNP64A1 burned grid cells had burn dates that matched the date of a MODIS active fire, versus 46 % for MCD64A1. For burn dates within two days of an active fire, the proportions were essentially identical. This global assessment was consistent with the results of regional intercomparison of VNP64A1 and MCD64A1 burn dates, which revealed that, for all years, the median difference in reported burn date was 0 days in every region, indicating no temporal bias between the products.

CRediT authorship contribution statement

Louis Giglio: Visualization, Supervision, Software, Project administration, Methodology, Investigation, Funding acquisition, Data curation, Writing – review & editing, Writing – original draft. **Luigi Boschetti:** Visualization, Validation, Methodology, Writing – review & editing, Writing – original draft. **David P. Roy:** Methodology, Writing – review & editing, Writing – original draft. **Joanne V. Hall:** Investigation, Data curation, Writing – review & editing. **Maria Zubkova:** Investigation, Data curation. **Michael Humber:** Software, Data curation. **Haiyan Huang:** Investigation, Data curation. **Vladyslav Oles:** Validation.

Funding

This work was supported by National Aeronautics and Space Administration grants 80NSSC21K1961 and 80NSSC21K1982.

Declaration of competing interest

The authors declare that they have no known competing financial

interests or personal relationships that could have appeared to influence the work reported in this paper.

Acknowledgements

We thank Andrés Santamaría-Artigas for his assistance with software and the processing of high-resolution diagnostic scenes, and four anonymous reviewers for their helpful comments and technical suggestions.

Appendix A. Supplementary data

Supplementary data to this article can be found online at https://doi.org/10.1016/j.rse.2025.115006.

Data availability

All data are freely available from NASA.

References

Archibald, S., Roy, D.P., van Wilgen, B.W., Scholes, R.J., 2009. What limits fire? An examination of drivers of burnt area in southern Africa. Glob. Chang. Biol. 15 (3), 613–630.

Bojinski, S., Verstraete, M., Peterson, T.C., Richter, C., Simmons, A., Zemp, M., 2014. The concept of essential climate variables in support of climate research, applications, and policy. Bull. Am. Meteorol. Soc. 95, 1431–1443.

Boschetti, L., Roy, D.P., 2008. Defining a fire year for reporting and analysis of global interannual fire variability. J. Geophys. Res. Biogeosci. 113 (G3).

Boschetti, L., Brivio, P.A., Gregoire, J.M., 2003. The use of Meteosat and GMS imagery to detect burned areas in tropical environments. Remote Sens. Environ. 85 (1), 78–91.

Boschetti, L., Flasse, S.P., Brivio, P.A., 2004. Analysis of the conflict between omission and commission in low spatial resolution dichotomic thematic products: the pareto boundary. Remote Sens. Environ. 91 (3–4), 280–292.

Boschetti, L., Brivio, P.A., Eva, H.D., Gallego, J., Baraldi, A., Grégoire, J.M., 2006. A sampling method for the retrospective validation of global burned area products. IEEE Trans. Geosci. Remote Sens. 44 (7), 1765–1773.

Boschetti, L., Roy, D.P., Justice, C.O., Giglio, L., 2010. Global assessment of the temporal reporting accuracy and precision of the MODIS burned area product. Int. J. Wildland Fire 19, 705–709.

Boschetti, L., Stehman, S.V., Roy, D.P., 2016. A stratified random sampling design in space and time for regional to global scale burned area product validation. Remote Sens. Environ. 186, 465–478.

Boschetti, L., Roy, D.P., Giglio, L., Huang, H., Zubkova, M., Humber, M.L., 2019. Global validation of the collection 6 MODIS burned area product. Remote Sens. Environ. 235, 11490.

Campagnolo, M.L., Sun, Q., Liu, Y., Schaaf, C., Wang, Z., Román, M.O., 2016. Estimating the effective spatial resolution of the operational BRDF, albedo, and nadir reflectance products from MODIS and VIIRS. Remote Sens. Environ. 175, 52–64.

Chuvieco, E., Englefield, P., Trishchenko, A.P., Luo, Y., 2008. Generation of long time series of burn area maps of the boreal forest from NOAA–AVHRR composite data. Remote Sens. Environ. 112 (5), 2381–2396.

Collins, L., Clarke, H., Clarke, M.F., McColl Gausden, S.C., Nolan, R.H., Penman, T., Bradstock, R., 2022. Warmer and drier conditions have increased the potential for large and severe fire seasons across South-Eastern Australia. Glob. Ecol. Biogeogr. 31 (10), 1933–1948.

Edwards, A., Russell-Smith, J., Meyer, M., 2015. Contemporary fire regime risks to key ecological assets and processes in north Australian savannas. Int. J. Wildland Fire 24 (6), 857–870.

Ellis, T.M., Bowman, D.M., Jain, P., Flannigan, M.D., Williamson, G.J., 2022. Global increase in wildfire risk due to climate-driven declines in fuel moisture. Glob. Chang. Biol. 28 (4), 1544–1559.

Franquesa, M., Lizundia-Loiola, J., Stehman, S.V., Chuvieco, E., 2022. Using long temporal reference units to assess the spatial accuracy of global satellite-derived burned area products. Remote Sens. Environ. 269, 112823.

Friedl, M.A., Sulla-Menashe, D., Tan, B., Schneider, A., Ramankutty, N., Sibley, A., Huang, X., 2010. MODIS collection 5 global land cover: algorithm refinements and characterization of new datasets. Remote Sens. Environ. 114 (1), 168–182.

Giglio, L., 2007. Characterization of the tropical diurnal fire cycle using VIRS and MODIS observations. Remote Sens. Environ. 108, 407–421.

Giglio, L., 2023. VIIRS/NPP Thermal Anomalies and Fire Daily L3 Global 1km SIN Grid V002 [data set]. NASA EOSDIS Land Processes Distributed Active Archive Center. Accessed 2024-07-16 from. https://doi.org/10.5067/VIIRS/VNP14A1.002.

Giglio, L., Roy, D.P., 2020. On the outstanding need for a long-term, multi-decadal, validated and quality assessed record of global burned area: caution in the use of advanced very high resolution radiometer data. Sci. Remote Sens. 2, 100007.

Giglio, L., van der Werf, G.R., Randerson, J.T., Collatz, G.J., Kasibhatla, P., 2006. Global estimation of burned area using MODIS active fire observations. Atmos. Chem. Phys. 6 (4), 957–974.

Giglio, L., Loboda, T., Roy, D.P., Quayle, B., Justice, C.O., 2009. An active-fire based burned area mapping algorithm for the MODIS sensor. Remote Sens. Environ. 113 (2), 408–420.

Giglio, L., Boschetti, L., Roy, D.P., Humber, M.L., Justice, C.O., 2018. The collection 6 MODIS burned area mapping algorithm and product. Remote Sens. Environ. 217, 72–85.

Giglio, L., Humber, M., Hall, J.V., Argueta, F., Boschetti, L., Roy, D.P., 2022. Collection 2 MCD64 Burned Area Collection 6.1 User's guide, Version 1.1. https://modis-fire.umd.edu/files/MODIS_C61_BA_User_Guide_1.1.pdf.

Giglio, L., Hall, J.V., Humber, M., Argueta, F., Boschetti, L., Roy, D.P., 2024. Collection 2 VIIRS Burned Area Product User's Guide, Version 1.1. https://lpdaac.usgs.gov/documents/2124/VNP64_User_Guide_v1.1.pdf.

Glaister, P., 2001. Least squares revisited. Math. Gaz. 85 (502), 104–107.

Hall, J.V., Argueta, F., Zubkova, M., Chen, Y., Randerson, J.T., Giglio, L., 2024. GloCAB: global cropland burned area from mid-2002 to 2020. Earth Syst. Sci. Data 16 (2), 867–885.

Jones, M.W., Abatzoglou, J.T., Veraverbeke, S., Andela, N., Lasslop, G., Forkel, M., Smith, A.J., Burton, C., Betts, R.A., van der Werf, G.R., Sitch, S., 2022. Global and regional trends and drivers of fire under climate change. Rev. Geophys. 60 (3), e2020RG000726.

Justice, C.O., Vermote, E., Townshend, J.R., Defries, R., Roy, D.P., Hall, D.K., Salomonson, V.V., Privette, J.L., Riggs, G., Strahler, A., Lucht, W., Myneni, R.B., Knyazikhin, Y., Running, S.W., Nemani, R.R., Wan, Z., Huete, A.R., van Leeuwen, W., Wolfe, R.E., Giglio, L., Muller, J.-P., Lewis, P., Barnsley, M.J., 1998. The moderate resolution imaging spectroradiometer (MODIS): land remote sensing for global change research. IEEE Trans. Geosci. Remote Sens. 36 (4), 1228–1249.

Justice, C.O., Giglio, L., Korontzi, S., Owens, J., Morisette, J., Roy, D., Descloitres, J., Alleaume, S., Petitcolin, F., Kaufman, Y., 2002. The MODIS fire products. Remote Sens. Environ. 83, 244–262.

Justice, C.O., Vermote, E., Privette, J., Sei, A., 2010. The evolution of US moderate resolution optical land remote sensing from AVHRR to VIIRS. In: Land Remote Sensing and Global Environmental Change: NASA'S Earth Observing System and the Science of ASTER and MODIS. Springer New York, New York, NY, pp. 781–806.

Justice, C.O., Román, M.O., Csiszar, I., Vermote, E.F., Wolfe, R.E., Hook, S.J., Masuoka, E.J., 2013. Land and cryosphere products from Suomi NPP VIIRS: overview and status. J. Geophys. Res. Atmos. 118 (17), 9753–9765.

Keeley, J.E., Syphard, A.D., 2021. Large California wildfires: 2020 fires in historical context. Fire Ecol. 17, 1–11.

King, M.D., Platnick, S., Menzel, W.P., Ackerman, S.A., Hubanks, P.A., 2013. Spatial and temporal distribution of clouds observed by MODIS onboard the Terra and Aqua satellites. IEEE Trans. Geosci. Remote Sens. 51 (7), 3826–3852.

Lin, G., Wolfe, R.E., Zhang, P., Dellomo, J.J., Tan, B., 2022. Ten years of VIIRS on-orbit geolocation calibration and performance. Remote Sens 14 (17), 4212.

Lizundia-Loiola, J., Otón, G., Ramo, R., Chuvieco, E., 2020. A spatio-temporal active-fire clustering approach for global burned area mapping at 250 m from MODIS data. Remote Sens. Environ. 236, 111493.

Lohr, S.L., 2022. Sampling: Design and Analysis, 3rd ed. Chapman and Hall/CRC, Boca Raton.

Masuoka, E., Roy, D.P., Wolfe, R., Morisette, J., Sinno, S., Teague, M., Saleous, N., Devadiga, S., Justice, C., Nickeson, J., 2011. MODIS land data products—Generation, quality assurance and validation, chapter 22 in Ramachandran. In: Justice, C.O., Abrams, M.J. (Eds.), Land Remote Sensing and Global Environmental Change—NASA'S Earth Observing System and the Science of ASTER and MODIS, Remote Sensing and Digital Image Processing Series, vol. 11. Springer, New York, pp. 511–534.

Morisette, J.T., Baret, F., Privette, J.L., Myneni, R.B., Nickeson, J.E., Garrigues, S., Kalacska, M., 2006. Validation of global moderate-resolution LAI products: a framework proposed within the CEOS land product validation subgroup. IEEE Trans. Geosci. Remote Sens. 44 (7), 1804–1817.

Olson, D.M., Dinerstein, E., Wikramanayake, E.D., Burgess, N.D., Powell, G.V., Underwood, E.C., D'Amico, J.A., Itoua, I., Strand, H.E., Morrison, J.C., Loucks, C.J., Allnutt, T.F., Ricketts, T.H., Kura, Y., Lamoreux, J.F., Wettengel, W.W., Hedao, P., Kassem, K.R., 2001. Terrestrial ecoregions of the world: a new map of life on earth a new global map of terrestrial ecoregions provides an innovative tool for conserving biodiversity. BioScience 51 (11), 933–938.

Roger, J.C., Ray, J.P., Vermote, E.F., Devadiga, S.D., 2023. Suomi-NPP VIIRS Surface Reflectance User's Guide, Version 2.0. https://lpdaac.usgs.gov/documents/1657/VNP09_User_Guide_V2.pdf.

Román, M.O., Justice, C., Paynter, I., Boucher, P.B., Devadiga, S., Endsley, A., Erb, A., Friedl, M., Gao, H., Giglio, L., Gray, J.M., Hall, D., Hulley, G., Kimball, J., Knyazikhin, Y., Lyapustin, A., Myneni, R.B., Noojipady, P., Pu, J., Riggs, G., Sarkar, S., Schaaf, C., Shah, D., Tran, K.H., Vermote, E., Wang, D., Wang, Z., Wu, A., Ye, Y., Shen, Y., Zhang, S., Zhang, S., Zhang, X., Zhao, M., Davidson, C., Wolfe, R., 2024. Continuity between NASA MODIS collection 6.1 and VIIRS collection 2 land products. Remote Sens. Environ. 302, 113963. https://doi.org/10.1016/j.rse.2023.113963.

Roy, D.P., 2000. The impact of misregistration upon composited wide field of view satellite data and implications for change detection. IEEE Trans. Geosci. Remote Sens. 38 (4), 2017–2032.

Roy, D.P., Boschetti, L., 2009. Southern Africa validation of the MODIS, L3JRC, and GlobCarbon burned-area products. IEEE Trans. Geosci. Remote Sens. 47 (4), 1032–1044.

Roy, D.P., Lewis, P.E., Justice, C.O., 2002. Burned area mapping using multi-temporal moderate spatial resolution data—a bi-directional reflectance model-based expectation approach. Remote Sens. Environ. 83 (1–2), 263–286.

Roy, D.P., Jin, Y., Lewis, P.E., Justice, C.O., 2005. Prototyping a global algorithm for systematic fire-affected area mapping using MODIS time series data. Remote Sens. Environ. 9, 137–162.

Roy, D.P., Lewis, P., Schaaf, C., Devadiga, S., Boschetti, L., 2006. The global impact of clouds on the production of MODIS bidirectional reflectance model-based composites for terrestrial monitoring. IEEE Geosci. Remote Sens. Lett. 3 (4), 452–456.

Roy, D.P., Huang, H., Boschetti, L., Giglio, L., Yan, L., Zhang, H.H., Li, Z., 2019. Landsat-8 and Sentinel-2 burned area mapping-a combined sensor multi-temporal change detection approach. Remote Sens. Environ. 231, 111254.

Roy, D.P., De Lemos, H., Huang, H., Giglio, L., Houborg, R., Miura, T., 2024. Multi-resolution monitoring of the 2023 Maui wildfires, implications and needs for satellite-based wildfire disaster monitoring. Sci. Remote Sens. 10, 100142.

Schroeder, W., Oliva, P., Giglio, L., Csiszar, I., 2014. The new VIIRS 375 m active fire detection data product: algorithm description and initial assessment. Remote Sens. Environ. 143, 85–96.

Tan, B., Woodcock, C.E., Hu, J., Zhang, P., Ozdogan, M., Huang, D., Yang, W., Knyazikhin, Y., Myneni, R.B., 2006. The impact of gridding artifacts on the local spatial properties of MODIS data: implications for validation, compositing, and band-to-band registration across resolutions. Remote Sens. Environ. 105, 98–114.

Tansey, K., Grégoire, J.M., Defourny, P., Leigh, R., Pekel, J.F., Van Bogaert, E., Bartholomé, E., 2008. A new, global, multi-annual (2000–2007) burnt area product at 1 km resolution. Geophys. Res. Lett. 35 (1).

van der Werf, G.R., Randerson, J.T., Giglio, L., van Leeuwen, T.T., Chen, Y., Rogers, B.M., Mu, M., van Marle, M.J.E., Morton, D.C., Collatz, G.J., Yokelson, R.J., Kasibhatla, P. S., 2017. Global fire emissions estimates during 1997–2016. Earth Syst. Sci. Data 9 (2), 697–720.

Vignesh, P.P., Jiang, J.H., Kishore, P., Su, H., Smay, T., Brighton, N., Velicogna, I., 2020. Assessment of CMIP6 cloud fraction and comparison with satellite observations. Earth Space Sci. 7 (2), e2019EA000975.

Wolfe, R.E., Roy, D.P., Vermote, E., 1998. MODIS land data storage, gridding, and compositing methodology: level 2 grid. IEEE Trans. Geosci. Remote Sens. 36, 1324–1338.

Wolfe, R.E., Lin, G., Nishihama, M., Tewari, K.P., Tilton, J.C., Isaacman, A.R., 2013. Suomi NPP VIIRS prelaunch and on-orbit geometric calibration and characterization. J. Geophys. Res. Atmos. 118 (20), 11–508.

Xu, W., Wooster, M.J., 2023. Sentinel-3 SLSTR active fire (AF) detection and FRP daytime product - algorithm description and global intercomparison to MODIS, VIIRS and Landsat AF data. Sci. Remote Sens. 7, 100087.